From half-cells to full-cells: across-scale comparative evaluation of lanthanum-based perovskites as high-performance anode materials for the oxygen evolution reaction

Blaž Toplak[a,§], Leon Müller[b,§], Ali Raza Khan[c], André Olean-Oliveira[c], Khuzaifa Yahuza Muhammad[d], Wang Feng[e], Raíssa Ribeiro Lima Machado[f], Da Xing[e], Mohammed-Ali Sheikh[b], Leander Kucklick[e], Ahammed Suhail Odungat[a], Philipp Gerschel[d], Corina Andronescu[f,g], Harry Hoster[e,g,h], Christof Schulz[b,g], Viktor Čolić[c,g], Ulf-Peter Apfel[d,i], Hartmut Wiggers[b,g], Mohaned Hammad[a,*], and Doris Segets[a,g,*]

[a] *Institute for Energy and Materials Processes – Particle Science and Technology, University of Duisburg-Essen, 47057 Duisburg, Germany*
[b] *Institute for Energy and Materials Processes – Reactive Fluids, University of Duisburg-Essen, 47057 Duisburg, Germany*
[c] *Electrochemistry for Energy Conversion, Max Planck Institute for Chemical Energy Conversion, 45470 Mülheim an der Ruhr, Germany*
[d] *Activation of Small Molecules – Technical Electrochemistry, Ruhr-Universität Bochum, 44801 Bochum, Germany*
[e] *Energy Technology, University of Duisburg-Essen, 47057 Duisburg, Germany*
[f] *Chemical Technology III, Faculty of Chemistry, University of Duisburg-Essen, 47057 Duisburg, Germany*
[g] *Center for Nanointegration Duisburg-Essen, University of Duisburg-Essen, 47057 Duisburg, Germany*
[h] *The Hydrogen and Fuel Cell Center ZBT GmbH, 47057 Duisburg, Germany*
[i] *Department of Electrosynthesis, Fraunhofer UMSICHT, 46047 Oberhausen, Germany*

[*]Corresponding authors.
E-mail addresses: doris.segets@uni-due.de (D. Segets), mohaned.hammad@uni-due.de (M. Hammad)

[§] These authors contributed equally to this paper.

ABSTRACT

The widespread reliance on evaluating electrocatalysts in electrochemical half-cells presents limitations that hinder a faster transition from academia to industry and can lead to premature exclusion of promising materials. To address these challenges, it is crucial to implement materials testing in application-relevant setups such as zero-gap full-cells. This transition can be achieved through implementing coherent workflows combining rapid evaluation of as-synthesized materials, electrode evaluation at different scales, and post-mortem analysis. This work presents a comparative study of three spray-flame synthesized lanthanum-based perovskite materials ($LaMnO_3$, $LaFeO_3$, and $LaCoO_3$) for the oxygen evolution reaction under alkaline conditions, highlighting different behavior across scales. The research demonstrates how the interplay of materials properties and electrode engineering affects performance under mild and harsh electrochemical conditions. Electrochemical half-cell testing consistently identifies $LaFeO_3$ as the best oxygen evolution reaction catalyst across various configurations. This unforeseen behavior necessitates further investigation under application-relevant conditions. Full-cell testing at 500 mA cm^{-2} confirms the trends observed in electrochemical half-cell testing, showing that even after prolonged operation, $LaFeO_3$ (2.09 V) and $LaMnO_3$ (2.16 V) maintain comparable performance and could potentially replace $LaCoO_3$ (2.07 V). Furthermore, advanced post-mortem techniques provide deeper insight into catalytic activity and structural changes, which cannot be fully explained without preliminary electrochemical half-cell testing. By linking fundamental studies to application-relevant testing, this research provides knowledge and methods for accelerated material and electrode development.

Keywords: zero-gap full-cell, coherent workflow, spray-flame synthesis, perovskite material, oxygen evolution reaction, alkaline water electrolysis

1. Introduction

Water electrolysis consists of water decomposition into hydrogen and oxygen through an external energy-driven redox reaction. The oxygen evolution reaction (OER), which occurs at the anode, is kinetically sluggish and represents a major bottleneck in the development of highly efficient anode electrocatalysts. Noble metals, such as Ir and Ru, exhibit adequate OER performance in acidic conditions. However, their scarcity, high cost, and limited stability hinder their practical applications [1,2]. In contrast, electrolysis in alkaline conditions can be performed with various non-noble metal materials with decent stability. Along this line, perovskite oxide materials (ABO_3, where A represents alkaline-earth or rare-earth metals {Ca, Sr, La} and B represents transition metals {Mn, Fe, Co, and Ni}) have shown promising results in alkaline OER [3–6]. For instance, La-based perovskites possess the advantage of structural flexibility in the A and B positions, which affects conductivity, stability, and defect formation [7].

In this study, we focus on three La-based perovskites: $LaMnO_3$, $LaFeO_3$, and $LaCoO_3$ (LMO, LFO, and LCO). The increase of the $Mn^{4+/3+}$ ratio in LMO induces more oxygen bonding with the active Mn^{4+}, leading to improved structural stabilization [8,9]. LFO combines good redox activity with suitable electronic and ionic conductivity [10]. However, LCO offers superior intrinsic catalytic activity compared to the other two candidates due to the $Co^{3+/4+}$ redox transitions, which promote the formation of oxygen vacancies in the lattice [7,11]. Although several OER studies have investigated previously mentioned perovskites [12–15], they have typically only been evaluated at laboratory-scale conditions using rotating disc electrodes (RDE) or on nickel foam at low current densities of 10 mA cm^{-2}, with LCO consistently presented as the best pristine perovskite for OER [12–14,16]. In these studies, the perovskite materials were prepared via solution combustion, sol-gel, or co-precipitation synthesis. However, all of these synthesis methods possess distinct drawbacks, including limitations in scalability, cost-efficiency, and control over particle phase, size, shape, and elemental

homogeneity, which results in low specific surface areas and hampers catalytic activity [17,18]. To tackle the aforementioned limitations, this work uses materials based on spray-flame synthesis and presents a direct comparison of La-based perovskite materials. Spray-flame synthesis has proven to be an efficient approach for the production of high-quality phase-pure perovskite nanomaterials with high specific surface and uniform primary particle size (x_p < 10 nm, derived from N_2 adsorption measurements), enabling their use in various applications such as anode materials in OER [19], water remediation [20], and selective CO oxidation [21].

Advancing technology for alkaline water splitting, and in particular for the OER, requires more than just understanding the intrinsic properties of the synthesized materials. It also involves addressing the associated challenges connected to anode preparation, which arise in the case of particle-based, coated catalyst layers from complex interactions between substrate, ionomer, and electrocatalyst. Factors such as ink formulation, ink deposition, substrate selection, and electrocatalyst properties influence adhesion, cohesion, wetting, and overall efficiency [22,23]. This creates a highly complicated system that requires a tailored approach for each electrocatalyst [19]. Another barrier is the slow transition from lab-scale testing in electrochemical half-cells (10-100 mA cm^{-2}, room temperature) toward industry-relevant testing using full-cells (≥ 500 mA cm^{-2}, ≥ 50 °C). This hinders the integration of the electrocatalysts into real-life systems early on in the product and process development due to a limited understanding of the material's behavior. To overcome these challenges, we previously developed a highly structured and coherent workflow that enables the evaluation of electrocatalyst performance (half- and full-cell testing) in combination with a systematic and trackable material assessment along the process chain, using scalable technologies [19]. This comprehensive approach integrates synthesis, advanced ink formulation, electrochemical testing, and electrode post-mortem analysis, pointing towards pathways for future materials development.

In this research, we emphasize two key aspects critical for further OER advancement. First, we highlight the importance of developing high-quality electrocatalysts and electrode engineering, which may lead to unforeseen performance of OER. Second, we emphasize the need for materials evaluation across scales to gain a comprehensive understanding of the active material's behavior during water electrolysis. By promoting the fast integration of full-cell testing conditions during the material development, we aim to enhance the insights gained from half-cell experiments. Hence, we intensively use electrochemical half-cell testing, as it provides crucial insights into intrinsic material properties that are difficult to obtain from industrial setups. However, we suggest complementing it with the material's exposure to testing conditions that are close to the later application. Bridging this gap can help avoid unjustified or premature elimination of promising materials after initial lab-scale testing. Additionally, incorporating post-mortem analysis strengthens the understanding of the mechanistic behavior of perovskites under harsh electrolyzer conditions, which will pave the way for the efficient design and engineering of next-generation electrocatalysts.

2. Experimental Section

2.1. Spray-flame synthesized perovskites

Nanomaterials applied for oxidation reaction tests were obtained by spray-flame synthesis. The setup consists of an in-house developed spray-flame reactor and a standardized SpraySyn burner [24], which is well described in preceding publications [25,26]. The liquid precursor is composed of metal acetates – $La(CH_3CO_2)_3 \cdot 1.5\ H_2O$ (Alfa Aesar, 99.9 %), $Mn(CH_3CO_2)_2 \cdot 4\ H_2O$ (Sigma-Aldrich, 99 %), $Fe(acac)_3$ (Sigma-Aldrich, 99 %), and $Co(CH_3CO_2)_2 \cdot 4\ H_2O$ (Sigma-Aldrich, reagent grade) – which were dissolved in a mixture (35:65 vol.%) of ethanol and 2-ethylhexanoic acid. A precursor with a total metal ion concentration of 0.2 mol L^{-1} was transferred with a constant feed rate of 2 mL min^{-1} to the nozzle of the SpraySyn burner. In the

nozzle, the precursor was brought into contact with the dispersion gas, a stream of mixed gases (1 standard liter per minute (slm) CH_4, 4.8 slm O_2), and formed a fine spray. To assure the stability of the flame and to avoid fluctuations in ignition, a premixed methane/oxygen flat flame (2 slm CH_4, 16 slm O_2) on a sintered bronze plate was used. The pilot flame was stabilized using a sheath gas flow (140 slm compressed air). An additional gas flow (240 slm compressed air) was used downstream of the flame for quenching and control of the off-gas temperature. The particles were precipitated on a fiber membrane filter and collected after synthesis was completed.

2.2. Characterization of perovskite nanopowders

A transmission electron microscopy (TEM) and a high-resolution TEM (HRTEM, JEOL JEM 2200FS) using 120000- and 500000-times magnification, equipped with energy-dispersive X-ray analysis (EDX) mapping was used to analyze the morphology, particle size, and elemental distribution. X-ray diffraction (XRD) patterns were recorded in the 2θ range from 10° to 90° (step size of 0.01°) using a Panalytical Empyrean diffractometer with Cu K_α (0.15406 nm) radiation. Raman spectroscopy measurements were performed using a Renishaw InVia Raman microscope equipped with 532 nm laser excitation (detection between 900 and 100 cm^{-1}). The X-ray photoelectron spectroscopy (XPS, ULVAC-PHI Versaprobe II, Chanhassen, USA) device was used to record powders applying an Al K_α radiation (hν = 1253.6 eV) with a band-pass energy of 11.75 eV. As a reference, the XPS spectra were calibrated using the C1s adventitious carbon C–C binding energy at 284.8 eV. All spectra were analyzed with the CasaXPS 2.3.25 software. Fourier transform infrared spectroscopy (FTIR) measurements were conducted using a spectrometer (Vertex 80, Bruker) between 4000 and 500 cm^{-1}. The N_2 adsorption measurements were performed using a Nova2000 device (Anton Paar) to determine the specific surface area of the samples using the Brunauer-Emmett-Teller (BET) method.

2.3. Characterization of dispersions

To ensure the reproducibility of HSP (Hansen solubility parameters, where in the case of powders the 'S' should be rather understood as similarity) values, procedures proposed by Süßet al., Bapat et al., and Anwar et al. [27–29] were employed. Dispersion stability measurements were performed using an analytical centrifuge (AC, LUM GmbH, Berlin, Germany) and were evaluated using transmission profiles and the AC software (SEPView 6.4.678.6069). The HSP sphere was determined using HSPiP software (5th Edition 5.4.08). Perovskite nanopowders were dispersed in different probe liquids with a 0.4 mg mL^{-1} concentration. Dispersions were prepared by sonication for 3 min using a sonication probe (Branson SFX 550 with a 3 mm sonication tip, 20% amplitude) in an ice bath. The energy input characteristics during the sonication process were obtained based on recommendations outlined in the NanoREG D4.12 SOP (supplementary material, Figure S1). Subsequently, 440 µL of the as-prepared dispersion was transferred into 2 mm AC cells and inserted into the AC. The measurements were carried out at 2000 rpm, 25 °C, and a wavelength of 410 nm.

2.4. Construction of catalyst electrodes on nickel plates and nickel foam

Inks composed of active materials in a concentration of 1 mg mL^{-1} were deposited onto nickel plates (purity: 99.2 %, HMW Hauner, 1×1 cm^2) and nickel foam (porosity: 95 %, purity 99.9 %, diameter: 4 cm, Goodfellow) using an ultrasonic spray coating system (Prism^{TM} 400 Ulra-Coat, USI Ultrasonic Systems Inc.). Before the coating process, the nickel substrates underwent cleaning using an ultrasonic bath (Elmasonic S, Elma) in Milli-Q water (Millipore purification system), 1 mol L^{-1} HCl, and acetone. The catalyst ink (40 mg) was prepared by 5 minutes of sonication (Branson SFX 550 using a 3 mm sonication tip, 20% amplitude) in 40 mL of water/ethanol mixture (75/25 v%). Subsequently, Sustainion® XA-9 ionomer (5 wt% in ethanol, Dioxide Materials) was added to the catalyst dispersion (concentration 5 µL of Sustainion® per mg of catalyst material), followed by further sonication for 5 min in an ice bath. The resulting

ink was sprayed over a nickel substrate heated to 150 °C in 40 coating runs, with an interval of 5 s between each consecutive spray. The final mass loading of the catalyst on the anode support was 250 μg cm^{-2}, determined gravimetrically.

2.5. Flow cell coupled with Inductively Coupled Plasma Optical Emission Spectroscopy (ICP-OES)

Inks composed of active materials were deposited onto polished nickel plates, polished Nickel RDE disks (purity: 99.2%, HMW Hauner, 0.5x0.5 cm), and polished glassy-carbon plates (purity 99.9%, 0.5x0.5 cm) using an ultrasonic spray coating system (Sono-Tek Corporation). Before the coating process, the nickel substrates underwent cleaning using an ultrasonic bath (Elamsonic S, Elma) in Milli-Q water (18.2 MΩ cm), 1 mol L^{-1} HCl, and acetone. Meanwhile, glassy carbon substrates were cleaned using an ultrasonic bath (Elmasonic S, Elma) in Milli-Q water (18.2 MΩ cm), 2-propanol, and acetone. The catalyst inks (20 mg) were prepared by 3 minutes of sonication (Branson SFX 550 using a 3 mm sonication tip, 20 % amplitude) in 20 mL of water/ethanol mixture (75/25 v%). Subsequently, Sustainion® XA-9 ionomer (5 wt% in ethanol, Dioxide Materials) was added to the catalyst dispersion (concentration 5 μL of Sustainion® per mg of catalyst material), followed by further sonication for 3 min in an ice bath. The resulting ink was sprayed over substrates heated to 150 °C in 160 coating runs, with an interval of 5 s between each consecutive spray. The final mass loading of the catalyst on the anode support was 1 mg cm^{-2}, determined gravimetrically.

2.6. Characterization of catalyst electrodes

The anodes' morphology was examined by scanning electron microscope (SEM, Nanoprobe 710, Ulvac-Phi) using an acceleration voltage of 5 kV and EDX (Quantax, Bruker) using an acceleration voltage of 20 kV. The morphology of the fabricated coatings was additionally inspected using an atomic force microscope (AFM, 30 x 30 μm, Tosca 400, Anton Paar). All topography measurements were conducted in non-contact mode using an AFM probe (ARROW-NCR-20) and analyzed with the Tosca Analysis 7.4 software. XRD patterns were recorded in the 2θ range from 15° to 80° (step size of 0.07°, compression cell) and from 20° to 70° (step size of 0.07°, full-cell) using a Rigaku Smartlab diffractometer with Cu K_α (0.15406 nm) radiation in grazing incidence mode (GIXRD). Raman spectroscopy measurements on electrode surfaces were performed using a Renishaw InVia Raman microscope equipped with 532 nm laser excitation (between 900 and 100 cm^{-1}, 77mW). The XPS spectra of perovskites coated on nickel foam were recorded using the (ULVAC-PHI Versaprobe II, Chanhassen, USA) device applying an Al Kα radiation (hν = 1253.6 eV) with a band-pass energy of 11.75 eV. As a reference, the XPS spectra were calibrated using the C1s adventitious carbon C–C binding energy at 284.8 eV. Subsequently, the resulting XPS spectra were analyzed using CasaXPS 2.3.25 software, with fitting carried out using a Shirley-type background and a Lorentzian lineshape. Contact angle measurements were performed using 1 mol L^{-1} purified KOH using a Dataphysics Contact Angle System OCA.

2.7. Electrochemistry

A standard protocol was employed for all electrochemical experiments to enable the comparison between the various electrocatalytic cells. The 1 mol L^{-1} KOH electrolyte was prepared using Milli-Q water with a resistivity of 18.2 MΩ cm and was further purified of metal cations using a Chelex®100 cation-exchange resin (Sigma Aldrich). All half-cell experiments were performed in O_2-saturated electrolyte at room temperature, while in the zero-gap full-cell, application-relevant conditions were simulated. All potential values measured in this study were converted to a reversible hydrogen electrode (RHE) scale using Eq. (1).

$$E_{iR}(RHE) = E_{Ag/AgCl} + E^{0}_{Ag/AgCl} + 0.059 \cdot pH - iR \quad (1)$$

Where E_{iR} (RHE) is the electrode potential compensated for the iR-drop in the RHE scale (V vs. RHE), $E_{Ag/AgCl}$ is the measured potential versus Ag/AgCl (3.4 mol L^{-1} KCl, in V), and $E^{0}_{Ag/AgCl}$ is the standard potential of the Ag/AgCl (3.4 mol L^{-1} KCl) reference electrode (0.21 V). The potentials were 85% automatically and 15 % manually iR-corrected using the uncompensated resistance (R, Ω), which was calculated by potentiostatic electrochemical impedance spectroscopy (PEIS) in the high-frequency range [19].

2.7.1. Scanning droplet cell

The electrochemical measurement of the Ni-plates coated with three different catalysts was executed using a high-throughput scanning droplet cell (SDC) purchased from Sensolytics GmBH, coupled with a Metrohm Autolab PGSTAT204 bipotenstiostat/galvanostat. The SDC electrochemical cell is composed of a three-electrode system, with a Pt coil as the counter electrode, an Ag/AgCl (3.4 mol L^{-1} KCl) as the reference electrode, and the working electrode formed upon contact of the SDC PTFE tip with the coated Ni-plate. The SDC cell is coupled to

a force sensor and is mounted on robotic arms for sealing and precise positioning of the cell over the electrode surface. Fresh electrolyte (O_2-saturated, 1 mol L^{-1} purified KOH) was provided for every measured area via a piston pump connected with PTFE tubes to the SDC cell. Before each measurement, the opening area of the PTFE tip of the SDC cell was measured with an optical microscope Di-Li 955 (Distelkamp). At each 1×1 cm^2 electrode, the electrochemical activity of the catalyst was measured at 25 individual spots, according to the following protocol: Initially, the open circuit potential (OCP) was recorded for 60 s. Afterward, 50 cyclic voltammograms were recorded (CV) with 100 mV s^{-1} in a potential range of 0.0 to 1.40 V vs. RHE. Subsequently, a linear sweep voltammogram (LSV) was recorded from 0.0 to 1.8 V vs. RHE with 5 mV s^{-1} with a stop-criterion of 50 µA. Lastly, electrochemical impedance spectroscopy (EIS) was measured at 0.0 V vs. OCP for 60 s, in a frequency range from 100 kHz to 1 Hz at 10 step dec^{-1}, with a sine wave of 10 mV (RMS) AC amplitude.[19] Statistical analyses of the current densities and overpotentials between the coated electrodes were evaluated using an ANOVA test by Past 4.0 software, with a level of significance set at a p-value ($p < 0.05$).

2.7.2. Rotating Disk Electrode

The RDE experiments were performed with a VSP-3e bipotentiostat (BioLogic, France) and a RDE rotator (PINE research, model: AFMSRCE, USA). Both polycrystalline nickel electrode (Ni – Ageo = 0.196 cm^2) and glassy carbon (GC – Ageo = 0.196 cm^2) electrodes (PINE research) were used as working electrode (WE), RHE (HydroFlex─Gaskatel) and a glassy carbon rod (HTW Hochtemperatur-Werkstoffe GmbH) and were used as a reference electrode (RE) and a counter (CE), respectively. Catalyst inks of 5 mg mL^{-1} were drop cast on the fresh polished electrode surface (using alumina powder following 1.0, 0.3, and 0.05 µm grain size) with a catalyst mass loading of 1 mg cm^{-2}. Afterwards, the electrodes were dried at room temperature for at least 60 min. The electrochemical protocol was based on the work [19]. EIS

spectra were recorded at OCP and 1.60 V vs. RHE applying a 10 mV sinewave from 30 kHz to 1 Hz, 10 step dec^{-1} to determine the uncompensated resistance for both iR-drop correction and charge transfer resistance, respectively. During the RDE measurement, 85 % iR-drop correction was applied automatically by the software EC-Lab. The remaining 15 % iR-drop correction was post-processed in OriginLab 2022.

2.7.3. Compression cell

Electrochemical measurements under a homogeneous potential distribution were performed using a compression cell [19,30]. A commercial hydrogen electrode (Gaskatel) was used as a reference electrode. To ensure its potential stability, the reference electrode was tested against a $Hg/HgSO_4$ (Na_2SO_4 sat.) before and after each experiment. Platinum mesh 1 × 3 cm^2 parallel to the working electrode as a counter electrode, and the Ni foil coated with the catalysts electrode used as a working electrode. The electrochemical protocol used was as follows: The electrode was stabilized by taking 50 CVs with a scan rate of 100 mV s^{-1} from 0.0 to 1.4 V vs. RHE. LSV at a scan rate of 5 mV s^{-1} was used to evaluate the electrochemical behavior, whereas chronopotentiometry with a current density of 10 mA cm^2 was used to investigate the electrochemical stability. EIS at OCP, from 30 kHz to 1 Hz, was performed and the spectra were fitted to the appropriate EEC to obtain the uncompensated resistance for iR-drop correction. Electrochemical and impedance spectra were collected using a computer-controlled VSP-300 potentiostat (BioLogic).

2.7.4. Flow cell coupled with ICP-OES

The electrochemical characterization of the catalyst-coated substrates was performed using a flow cell combined with an ICP-OES. The ICP flow rate was either 1.5 or 4 mL min^{-1}. Standard solutions for La, Mn, and Co were prepared by diluting the ICP standard (Sigma-Aldrich) using 1 mol L^{-1} KOH. A leak-free Ag/AgCl (3.4M KCl) electrode (innovative instruments)) was used

as the reference electrode, and a Pt coil was used as the counter electrode. In the closed-type flow cell, a polypropylene separator membrane (Celgard 3401) was used. The membrane separating the working and counter-electrode compartments of the cell, together with the O-rings, was replaced every few weeks as the polymer stretched to ensure that contamination did not build up. New membranes were punched out using a 10 mm diameter punch and die. The cell was periodically disassembled and placed in an acid bath of 2–5 % nitric acid for a few hours before being thoroughly rinsed with Milli-Q water (18.2 MΩ cm). Downstream of the working electrode, PTFE tape was sometimes used to replace Delrin ferrules with similar results. Parafilm was also found to be very effective as a ferrule material. The counter electrode was replenished each day of the experiment with 1 mol L^{-1} KOH. Otherwise, pH differences between the counter electrode compartment and the flow compartment could increase due to CO_2 absorption from alkaline solutions.

2.7.5. Full-cell testing

The experiments were carried out in a custom-made two-electrode zero-gap cell using a Gamry Reference 3000 potentiostat equipped with a Booster (Gamry) unit. For the anode side, a 0.40 mm thick PTFE sealing and for the cathode side, a 0.15 mm thick PTFE sealing was used. The membrane electrode assembly (MEA) applied in the full-cell measurements consisted of the individual catalyst-coated nickel foams (40 mm diameter, 0.4 mm thickness) as an anode, and a PiperION-HCO3 membrane (40 µm thickness) conditioned for at least 24 h in 1 mol L^{-1} KOH as anion exchange membrane and an H23 (Freudenberg) carbon paper coated with platinum, nominally 40 % on carbon black (2.9 mg cm^{-2}, 1.0 mg Pt cm^{-2}) loading, 10 wt% Sustainion® XA-9 binder, 40 mm diameter, 0.15 mm thickness) applied with an Eclipse Airbush pistol (Iwata). This placement is crucial for minimizing the contribution of cell resistance arising from both the electrolyte and the formation of bubbles during oxygen and hydrogen evolution. The voltage in the electrochemical cell depends on the spacing between the

electrodes, where the gapless system promotes high efficiencies [31,32]. Prior to applying the platinum to the carbon paper, which was heated to 110 °C on a hotplate, the ink was ultrasonicated for 10 min (VWR USC-T, ultrasonic frequency approx. 45 kHz) and afterward further dispersed using a T-25 Ultra-Turrax operating at 13400 rpm for 2 mins. The cathode consisted of 1.0 mg cm^{-2} of platinum. The dry weight of the catalyst also included 10 wt% Sustainion® XA-9 binder (Dioxide Materials), which was added as 5 wt% dispersion in ethanol to an ink consisting of 6:1 volumes of isopropanol and water. The Ni-foam anodes (porosity: 95%, purity: 99.9%, Goodfellow) were compressed from 1.6 mm thickness to 0.4 mm using a hydraulic press before coating. For the polarization curve measurements, 20 s long multi-step chronopotentiometries held at the corresponding current densities were recorded. Before the 12 h chronopotentiometries held at 0.5 A cm^{-2} were initiated, a 1 h conditioning at the same current density was performed.

3. Results and discussion

3.1. Catalytic nanopowder characterization

All three perovskite materials were synthesized using spray-flame synthesis with identical solvents and concentration ratios of the respective precursors. Their structures and compositions were analyzed using X-ray diffraction (XRD, Figure 1a) and Raman spectroscopy (Figure 1b). LMO and LFO diffraction peaks can be indexed to the single-phase orthorhombic structure matching ICSD 51653 and ICSD 7794, respectively [33–36]. Conversely, the diffraction pattern of LCO matches the rhombohedral perovskite $LaCoO_{2.925}$ structure (ICSD 153993) [15]. The phase compositions of the perovskite materials were additionally assessed with Raman spectroscopy at room temperature, which has the advantage of being more sensitive to oxygen motion and structure distortion [37,38]. The Raman spectra of LMO reveal two strong vibrational modes at around 495 and 622 cm^{-1}, which are attributed to the Jahn-Teller distortion of MnO_6 octahedra [39,40]. Likewise, in the LFO, Raman modes at 435 cm^{-1} are related to

oxygen bending vibrations, while stretching Raman modes of FeO_6 octahedra are observed at 636 cm^{-1}. These findings for both materials are consistent with the orthorhombic structural configuration previously determined through XRD [41–43]. Furthermore, the Raman mode in LCO at 640 cm^{-1} corresponds to Co–O stretching vibrations, providing additional support for the rhombohedral arrangement of LCO [44,45].

To investigate the surface properties and valence states of all three perovskite powders, X-ray photoelectron spectroscopy (XPS) analysis was performed. In all cases, lanthanum (supplementary material, Figure S2a) is present as La^{3+}. The La $3d_{5/2}$ multiplet splitting shows energy differences of 3.7, 3.7, and 3.8 eV for LMO, LFO, and LCO, respectively. These values are consistent with those reported in the literature for lanthanum-based perovskites [46,47]. The surface spectra of Mn $2p_{3/2}$ (supplementary material, Figure S2b) deconvoluted by peaks at 641.1 and 642.8 eV, belong to Mn^{3+} and Mn^{4+} species, where manganese is predominantly in the Mn^{3+} valence state [48]. The two Fe $2p_{3/2}$ peaks (supplementary material, Figure S2c) positioned around 710.2 and 711.9 eV indicate the presence of a mixed oxidation state of Fe^{2+} and Fe^{3+}, respectively [49]. The Co $2p_{3/2}$ (supplementary material, Figure S2d) spectra are also fitted with two individual peaks at 779.7 and 781.4 eV, corresponding to the Co^{3+} and Co^{2+} oxidation states [50,51]. The main O 1s XPS spectra for all materials were deconvoluted into two components (supplementary material, Figure S2e) at around 528.8 and 531.5 eV, respectively, indicating predominantly lattice oxygen ($O_{lattice}$) and adsorbed hydroxyl species ($O_{surface}$) on the surface [51,52].

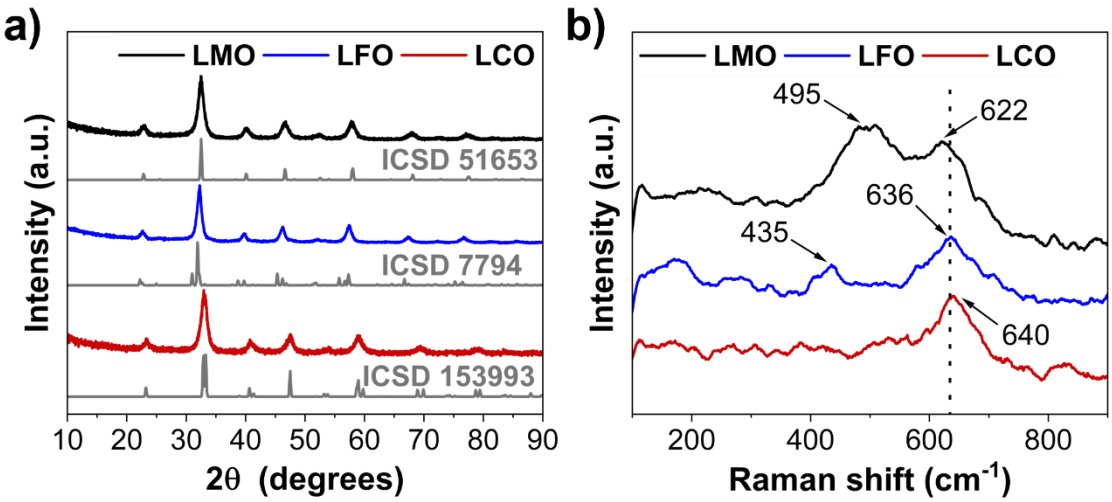

Figure 1. (a) XRD patterns of spray-flame synthesized LMO (black), LFO (blue), and LCO (red), with corresponding ICSD references 51653, 7794, and 153993 (grey). (b) Raman spectra of LMO (black), LFO (blue), and LCO (red).

The morphological and elemental analysis of spray-flame synthesized perovskite materials was performed using transmission electron microscopy (TEM) and energy dispersive X-ray mapping (EDX) (Figure 2a–c, supplementary material, Figure S3a–c). All three materials are confirmed to be mainly present as quasi-spherical primary nanoparticles with distinct edges, while the EDX analysis evidences a uniform elemental distribution in all three perovskites. Furthermore, high-resolution TEM (HRTEM) images of LMO and LFO (Figure 2d–e) show interplanar spacing of 0.281 nm for LMO, corresponding to the (011) orthorhombic lattice plane, and 0.285 and 0.395 nm for LFO, matching the (121) and (101) lattice planes, respectively [20,53]. Moreover, the HRTEM image of LCO (Figure 2f) exhibits crystal lattice fringes with an interlayer spacing of 0.273 nm, corresponding to (104) rhombohedral planes, consistent with the XRD and Raman spectroscopy analysis [54,55]. Additionally, the specific surface area was examined using the BET method. The measured specific surface of LMO, LFO, and LCO were 105.2, 94.2, and 84.6 m^2 g^{-1}, with corresponding calculated primary particle sizes (d_p^{BET}) of 8.7, 9.6, and 10.0 nm, respectively.

In total, combining all structural and surface characterizations confirmed that all three nanopowders possess phase-pure perovskite structures with high surface area, which is crucial for enhancing the accessibility of active sites.

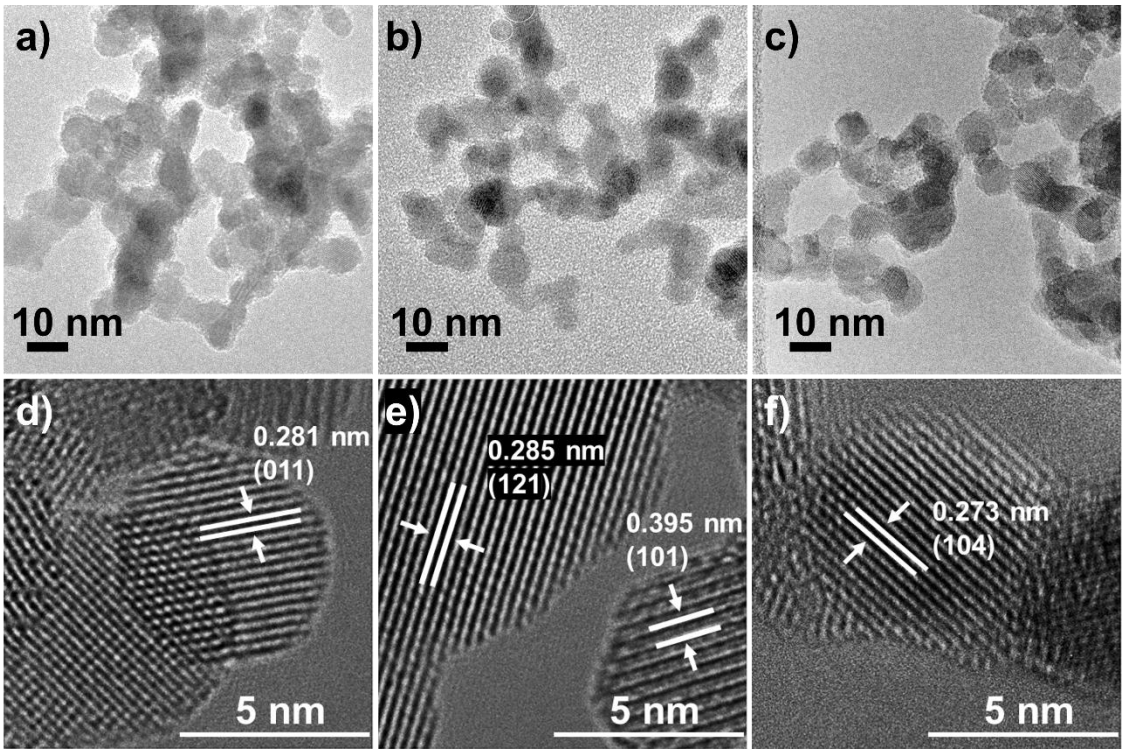

Figure 2. TEM images of LMO, LFO, and LCO nanopowders (a, b, and c). HRTEM images of LMO, LFO, and LCO perovskite materials (d, e, and f).

3.2. Powder wetting, dispersion, and ink characterization

Understanding interactions between nanoparticles, additives, and solvents is important for efficient electrode fabrication and the successful transition from lab-scale to larger-scale processes. The key to a smooth transition is the preparation of homogeneous and stable dispersions from non-toxic, environmentally and economically feasible solvents and additives/binders. To investigate interactions of LMO, LFO, and LCO nanoparticles with different solvents or probe liquids (PLs), the method of HSP was utilized, which was adopted by us to assess particulates [56,57]. Thereby, the selection of PLs plays a crucial role in

determining the surface properties of perovskite nanoparticles. For that reason, a two-step method developed by Amin et al. [58] was introduced. LMO, LFO, and LCO were initially dispersed in polar protic, polar aprotic, and moderate polar PLs, including ethanol, dimethylformamide, tetrahydrofuran, 2-propanol, dimethylsulfoxide, and acetone. The interactions and stability of perovskite nanoparticles in the PLs were visualized using transmittograms (supplementary material, Figure S4–S6), which provide the qualitative and quantitative characteristics of the physical properties of complex colloidal or dispersed systems [59]. For the calculation of the HSP sphere, the interaction of perovskites with different PLs were finally categorized on the basis of relative sedimentation times of the settling dispersion during analytical centrifugation. Using the HSPiP software and the automated addition method developed by Süß et al. and Anwar et al., the ordering of PLs into good and poor was done (supplementary material, Figure S7) [28,29]. Transmittograms reveal similar interactions in LMO and LFO, resulting in the same PL ranking and HSP. Both materials demonstrate good dispersibility in polar protic ethanol and 2-propanol, as well as polar aprotic dimethylformamide. In contrast, moderate polar PLs tetrahydrofuran, acetone, and polar aprotic dimethylsulfoxide, are classified as poor. LCO shows good dispersion stability in polar protic ethanol and polar aprotic dimethylformamide and dimethylsulfoxide, while 2-propanol, tetrahydrofuran, and acetone were classified as poor. Differences in HSP are explained by distinct crystal structures, which affect the interactions between the nanoparticle surface and the probe liquid molecules [56,60,61]. These differences are reflected in the elevated δ_D and δ_P values of LCO compared to LMO and LFO, resulting in a larger radius of the Hansen sphere (supplementary material, Figure S7, Table S1).

For further understanding of the interaction between perovskites and PLs, Fourier-transform infrared spectroscopy (FTIR) measurements (supplementary material, Figure S8) of powders were performed. Vibration modes at 850 cm^{-1} in all three materials are associated with Mn−O, Fe−O, and Co−O vibrations [62,63]. The presence of vibration modes between 1300 and 1600

cm^{-1} indicates the presence of organic residues on the surface after spray-flame synthesis. The vibrations in LMO and LFO samples at 1372 and 1479 cm^{-1} are related to the C−H vibration modes [64,65], while additional vibrations noticed just in LMO at 1420 and 1578 cm^{-1} are attributed to C−H and C=C bonds [66]. Vibrational modes in LCO appear at 1315, 1420, and 1530 cm^{-1}, corresponding to O−C=O, O−H, and C=C vibrations [64,65]. Above 3000 cm^{-1}, it is noted that LMO and LFO possess a significantly higher amount of surface O−H groups than the LCO particles, which correlates perfectly with the HSP data [64].

Based on the HSP, ethanol was found as a suitable continuous phase for dispersing the three perovskites and was selected as the solvent for the subsequent ink formulation. However, ethanol is a common solvent used in various applications and technological processes, resulting in a massive demand, which has led to increased prices over the last few years [67,68]. Lowering production costs can be achieved by introducing water into the system [68–73]. In contrast to inks solely based on ethanol, the use of water/alcohol mixtures has been observed to impede crack formation and the occurrence of film delamination during drying, mainly stemming from the rapid evaporation of ethanol at elevated temperatures [74,75]. Therefore, stability characterization of the catalysts in ethanol, water, and various mixtures of water/ethanol (50/50, 75/25, and 90/10 v/v%) was conducted (supplementary material, Figure S9–S11). Results for all three perovskites show a similar trend of reducing the stability of dispersions and faster material sedimentation with the increasing concentration of water. According to the results on dispersion stability, a water/ethanol mixture of 75/25 v/v% is selected as the continuous phase for further formulations, as it presents a good compromise between costs and stability (Figure 3a–c).

Upon selecting the suitable solvent, inks were formulated by the incorporation of Sustainion® as a binder. Our previous findings indicate that incorporating fluorine-free Sustainion® in the electrode preparation of $La_{0.8}Sr_{0.2}CoO_3$ and $NiFe_2O_4$ nanomaterials significantly improved electrode durability, enhancing their performance in the OER [19]. As demonstrated in all cases

(Figure 3d–f), the addition of Sustainion® in small concentrations improved the ink stability, resulting in decreased sedimentation over time.

Altogether, we believe that this structured process for ink development and improvement will play an important role in scale-up reproducible electrode fabrication.

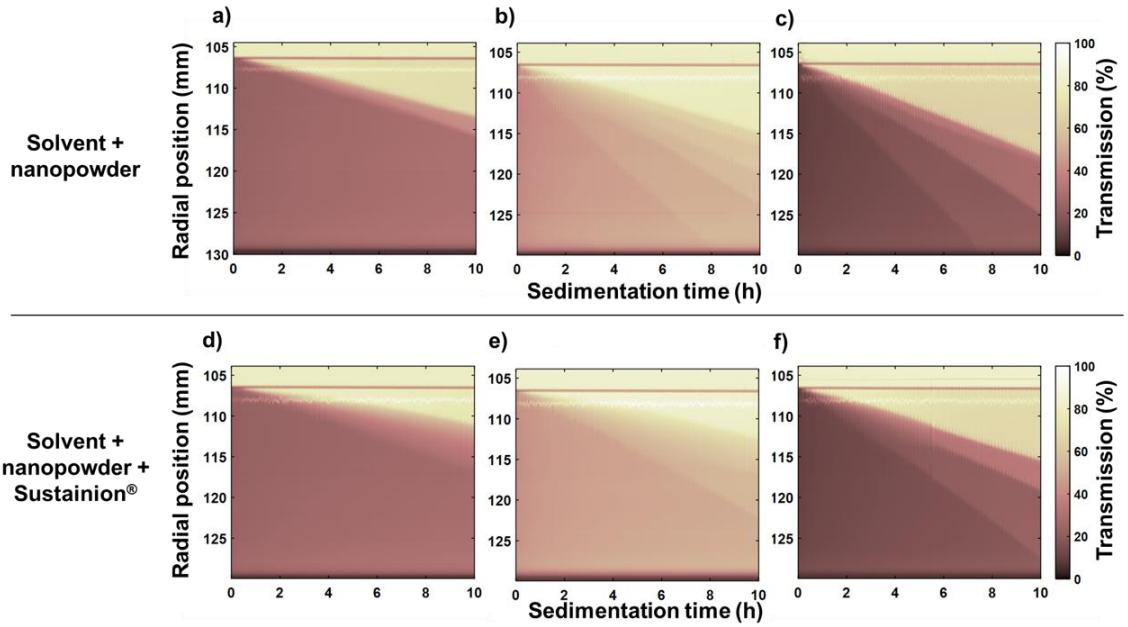

Figure 3. Transmittograms of LMO, LFO, and LCO dispersions in H_2O/EtOH 75/25 v/v% (a, b, and c). Transmittograms of LMO, LFO, and LCO inks with Sustainion® binder in H_2O/EtOH 75/25 v/v% (d, e, and f). Darker colors present low transmission and better phase stability over time.

3.3. Structural characterization of catalyst-coated nickel-substrate anode electrodes

The surface morphology and roughness of the LMO-, LFO-, and LCO-based thin-film electrodes were assessed using a SEM, EDX, and AFM. The SEM measurements (Figure 4a–c) confirm that all three electrodes exhibit smooth and slightly porous structures, while EDX analysis indicates uniform elemental distribution across all electrodes. This includes the organic component from the Sustainion® binder (supplementary material, Figure S12–S14), indicating

good dispersibility in a water/ethanol environment. Furthermore, AFM (Figure 4d–f) was employed to analyze surface characteristics represented by the square mean root roughness (Sq) values. The Sq values assessed for LMO-, LFO-, and LCO-based electrodes are situated between 155 – 180, 160 – 200, and 180 – 220 nm, respectively. The slight rise in surface roughness can be attributed to the increased perovskite nanoparticle size from LMO towards LCO, as confirmed by TEM and BET analysis. The increase in particle size can also explain the increase in pore surface coverage and average pore size distribution from LMO towards LCO (Table 1**,** supplementary material, Figure S15–S16). It is worth noting that surface roughness and porosity affect the presence of active sites, mass transport, and catalytic performance [23,76–78]. Therefore, additional contact angle measurements were performed (supplementary material, Figure S17), where no significant differences were observed, underpinning constant wetting properties across all three anode materials.

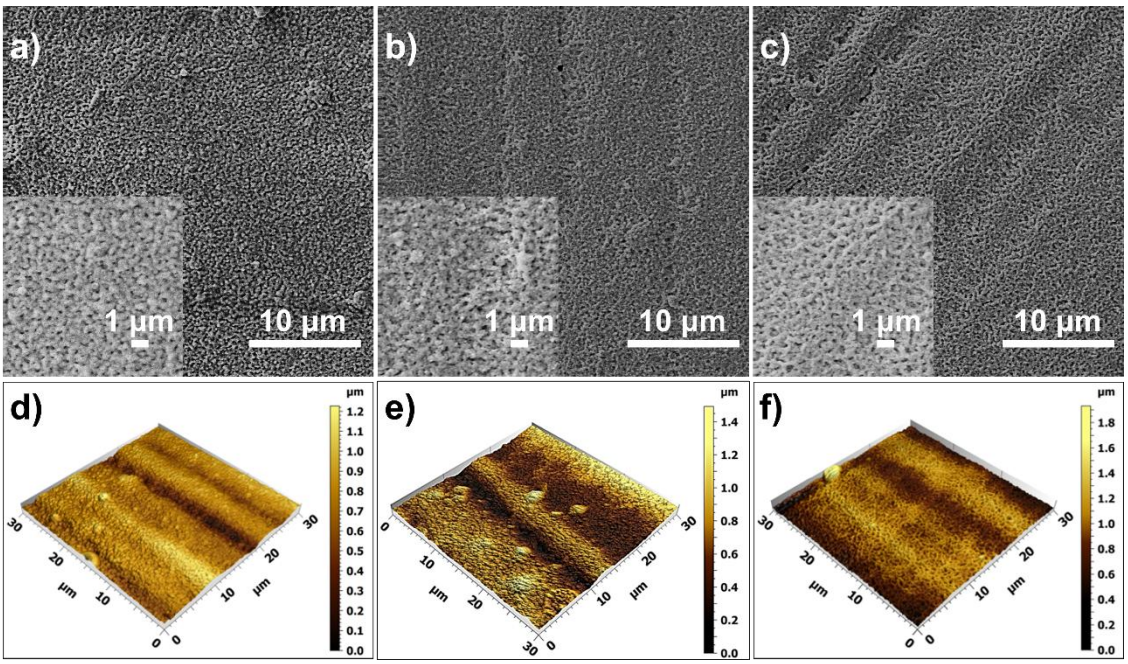

Figure 4. SEM images of electrodes made by spray-coating of Sustainion®-containing LMO-, LFO-, and LCO-based inks on nickel substrates (a-c). AFM topography images of LMO-, LFO-, and LCO-based electrodes (d-f).

To summarize, Table 1 presents the most important parameters for OER. Taking into account the powder synthesis and electrode engineering of our catalysts (including ink formulation, electrode fabrication, and surface characterization), we can conclude that our methodology enables fast, reproducible, and scalable electrode manufacturing. The synthesized powders exhibit similar properties, with a slightly higher surface roughness and porosity of the LCO-based electrodes. As expected, the combination of comparable synthesis conditions and electrode engineering enables the generation of anodes for which the OER performance will be primarily connected to intrinsic properties of the active material rather than to the structure-driven electrolyte wettability.

The prepared electrodes will be electrochemically evaluated in the next sections using different electrochemical techniques to investigate how the combination of intrinsic material and electrode properties affects the OER performance.

Table 1. Powder and electrode parameters relevant for the OER performance

Nanopowder parameters			
x_p^{BET} / nm	8.7	9.6	10.0
BET / $m^2\ g^{-1}$	105.2	94.2	84.6
XPS / [$O_{surface}$ /$O_{lattice}$]	0.83	0.94	0.90
HSP			
$\delta_D/\delta_P/\delta_H/R$ / $Mpa^{0.5}$	16.5/10.7/15.0/5.1	16.5/10.7/15.0/5.1	17.1/12.6/14.9/6.6
Electrode parameters			
Sq roughness / nm	155 – 180	160 - 200	180 – 220
Surface pore coverage / %	8.6	8.8	10.6
Contact angle / °	85	89	91

3.4. Electrochemical characterization of catalyst-coated electrodes

3.4.1. Scanning droplet cell tests

The lateral homogeneity of the 1 × 1 cm^2 nickel (Ni)-plates coated with 250 µg cm^{-2} LMO, LFO, and LCO with Sustainion® as a binder was assessed by SDC, analysis (supplementary material, Figure S18). For each coated electrode, the electrocatalytic activity was evaluated based on 25 measured areas that were analyzed and spaced 1.8 mm apart (supplementary material, Figure S19, spot area of 0.0021 ± 0.0002 cm^2). Figure S20 (supplementary material) presents the average and standard deviation of the LSVs. LFO-based electrodes exhibit the lowest overpotential value (η) for OER at 10 mA cm^{-2} (1.541 ± 0.002 V vs. RHE) of the investigated catalyst-coated electrodes. At the same current density, the LCO-based electrodes follow with an inferior activity (1.560 ± 0.003 V vs. RHE), while the lowest activity among the coated electrodes is observed for the LMO-based electrodes (1.635 ± 0.007 V vs. RHE). The differences in overpotential among the electrodes were statistically significant ($p < 0.05$).

The homogeneity of the coatings for OER activity is also represented in the activity maps (supplementary material, Figure S21a–b). The current densities of the 25 individual measured areas of each coated electrode and their relative standard deviation compared to the average of the sample across the spots are represented at a potential of 1.541 V vs. RHE. LFO-based electrodes (8.8 mA cm^{-2}) exhibited a superior average current density compared to LCO-based electrodes (7.4 mA cm^{-2}) and lastly to the LMO-based electrodes (4.9 mA cm^{-2}). The homogeneity of the OER activity is also evident in the standard deviations of ±16.4, ±11.6, and ±7.6 % of LMO-, LFO-, and LCO-based electrodes, along with their respective maximum deviations of 42.1, 25.6, and 16.3 %, respectively. Despite the coated films appearing visually homogeneous before the SDC measurements (supplementary material, Figure S22), the LMO-based electrode surface was more damaged after measurements due to the additional force needed to seal the SDC and prevent electrolyte leakage. This result aligns with previous reports

indicating that LMO exhibits less efficient activity compared to LCO and $LaMn_xCo_yO_3$-based perovskites [79,80].

In brief, the homogeneity of electrochemical activity for OER was successfully investigated using high-throughput SDC. This automated, versatile, and efficient technique enables precise screening of electrode surfaces, thus providing preliminary data to support and accelerate the development and scaling up of new electrocatalysts. However, at this point, the superior performance of the LFO-based electrodes compared to LCO- and LMO-based electrodes raises additional questions, which are discussed in the next section.

3.4.2. Rotating disc electrode, compression cell, and flow cell coupled with inductively coupled plasma-optical emission spectrometry (ICP-OES) experiments

In the scaling-up process, accurately determining the electrocatalytic activity is essential for identifying promising candidates and discarding materials with insufficient performance. Electrochemical evaluation typically includes RDE measurements (supplementary material, Figure S23), with glassy carbon (GC) being the most commonly used support material. This is often followed by tests on three-dimensional (3D) metal-based supports, such as Ni foam [19]. As highlighted in our previous study, an important consideration is the potential impact of support-catalyst interactions on the catalyst's performance, which could affect its activity [81,82]. To investigate this further, we performed electrochemical measurements in the RDE system using both GC and Ni as support materials, where the induced rotation reduced mass transport limitations and facilitated oxygen bubble removal [83]. Figure 5a-b presents the activity of LFO, LCO, and LMO deposited on a GC and Ni electrode support in a conventional RDE system. The observed trends were similar for both systems, except for the LMO-based electrode, which showed no electrocatalytic activity when GC was used as the support material.

In general, the potential values recorded at 10 mA cm^{-2} presented higher overpotentials when the GC was employed as the support.

Subsequently, EIS measurements were conducted at a potential of 1.6 V vs. RHE to gain further insight into the electrochemical behavior, as shown in Figure S24a–c (supplementary material). The Nyquist plot revealed significant differences in the charge transfer resistance (R_{ct}) based on the capacitive arc diameter. For instance, the LFO-based electrode exhibited an $R_{ct} \approx 6\ \Omega$ for Ni-coated electrodes and 235 Ω for GC-coated electrodes. The higher value of R_{ct} observed for GC can be attributed to the potential dissolution/deactivation of LMO and inactivity towards OER.

Notably, for the LCO-based electrode, two distinct capacitive arcs were observed, indicating two processes with different time constants at the catalyst layer/electrode interface, due to differences in capacitive and resistive properties when Ni is used as the support electrode [84]. This second time constant is evident in the Bode plot (supplementary material, Figure S25a–b,), which shows two peaks at approximately 3000 and 10 Hz. The additional interface may affect the electrocatalytic activity by introducing electron transfer from the catalyst to the electrode or by charging the interface through accumulating charge. In contrast, the LFO- and LMO-based electrodes exhibit a single time constant. Further investigation will be carried out in a dedicated study for a better understanding.

Additional support for the improved intrinsic properties of the LFO-based electrode in relation to the OER performance can arise from prior density theory calculations. Tripkovic et al. [85] correlated higher overpotential of LCO to changes related to the valence state of the metal center and differences in the number of hydroxyl species on the surface. This is experimentally validated with our XPS results, where the LFO shows the highest hydroxyl group surface coverage ratio (Table 1).

The compression cell (supplementary material, Figure S26) enables the exposure of the electrode surface area to the electrolyte under uniform potential distribution across the exposed

area [30]. During the measurements, the oxygen is not removed and remains in close vicinity of the electrode [19]. LSV measurements (supplementary material, Figure S27) of electrocatalysts at 10 mA cm^{-2} revealed that the LFO-based electrodes demonstrated the best performance, achieving 1.54 V vs. RHE, closely followed by the LCO-based electrodes with 1.57 V vs. RHE, aligning well with the SDC results. In contrast, the LMO-based catalyst performed significantly worse, with a value of 1.73 V vs. RHE, compared to the other two materials. This is partially attributed to the electrochemical surface area (ECSA, supplementary material, Figure S28a–d, Table S2–S3), which is significantly lower compared to LFO- and LCO-based electrodes (0.30, 0.57, and 0.55 cm^2). After approximately 41 mA cm^{-2}, a crossover point in the LSV-curves of the LFO- and LCO-based electrodes is observed. This could be attributed to two possible scenarios. The first is related to the configuration of the electrochemical cell, and the second is the activation of the LCO-based electrodes connected to material segregation [86]. These hypotheses will be evaluated in the following through post-mortem analysis following long-term stability testing. Subsequent chronopotentiometric stability (CP) measurements (Figure 5c) were performed at 10 mA cm^{-2} for 12 h. The same trend was noted from the LSV across the whole measurement window. During the measurement period, LFO-, LCO-, and LMO-based electrodes showed a slight increase from their initial potential to 1.56, 1.59, and 1.85 V vs. RHE, respectively. Furthermore, low standard deviations of LFO- and LCO-based electrodes suggest good reproducibility of these electrodes under laboratory conditions.

Following the compression cell measurements, post-mortem morphological and elemental evaluations were conducted using EDX, SEM, and AFM. The EDX analysis (supplementary material, Figure S29–S31) exhibits uniform elemental distribution. SEM images (supplementary material, Figure S32a–c) reveal that all electrodes maintain a homogeneous coating after their exposure to the electrochemical treatment, with some randomly allocated agglomerates. However, in the case of LCO-based electrodes, surface cracks are observed post-

electrochemical testing. The AFM analysis (supplementary material, Figure S32d-f), conducted after stability testing for 12 h, shows a reduction in the Sq values, while the trend amongst different materials remains as observed in the case of the pristine electrodes. Among the electrocatalysts, LMO-based electrodes exhibit the smoothest surface with minimal variations across the area. The Sq values range between 85 – 95 nm, followed by LFO-based electrodes, with Sq values between 110 –130 nm. The LCO-based electrodes display the highest Sq values, ranging from 140 – 180 nm, respectively. Similarly to the SEM, AFM also revealed cracks on the surface of LCO-based electrodes, which indicates and supports the hypothesis on material-segregation that was deduced from the crossing of the LSV-curves in Figure S27 (supplementary material). Moreover, grazing-incidence X-ray diffraction (GIXRD) was employed to investigate the potential changes in the crystal phase after compression cell measurements (12 h at 10 mA cm^{-2}). While GIXRD (Figure S33a–c) did not reveal any significant phase changes in LMO-, LFO-, and LCO-based electrodes after electrochemical stress, the strong diffraction signals from the nickel substrate likely masked subtle structural modifications in the perovskite phases, potentially limiting the detection of minor phase transformations.

Overall, structural characterization under laboratory conditions did not reveal significant changes in the electrode surface morphology and composition. This good structural stability is crucial before subjecting the materials to harsher conditions, as unstable materials should not be considered for further testing at application-conditions [19].

Integrating the electrochemical cell with ICP-OES (supplementary material, Figure S34) enables the direct analysis of reaction products and establishes a link between dissolution behavior and the electrochemical operation [87]. The configuration plays a vital role in regulating transport processes, including diffusion, convection, and migration of reactive products and bubbles away from the electrode. Additionally, it introduces mechanical stress on the electrode surface, facilitating the investigation of the electrochemical stability [88].

During these measurements, a minor transient of Fe and Mn dissolution (supplementary material, Figure S35a) is observed, independent of the applied potential. The leaching behavior of the metal ions is summarized in Figure S35b (supplementary material). During OER operation, Fe and Mn dissolution is detectable at a current density of 5 and 10 mA cm^{-2}, resulting in approximately 0.25 ng s^{-1} cm^{-2} for Fe and 0.68 ng s^{-1} cm^{-2} for Mn. The dissolution rate of Fe increases transiently and slowly decreases until the end of the hold. The calculated dissolution should be treated with caution under these operating conditions, as it is below the nominal detection limit of the online ICP-OES system. However, manganese leaching may be a partial reason for the poor electrochemical performance of LMO-based electrodes, as discussed previously during RDE measurements. Furthermore, no La or Co dissolutions are observed during OER operation at steady-state current.

In conclusion, the OER performance of perovskite catalysts was systematically evaluated using three different complementary lab-scale electrochemical techniques, providing in-depth insights into their performance at low current densities. The findings are in good agreement with the previously used SDC technique. Our results are in sharp contrast with the previously mentioned studies from the literature that identified LCO powder as the most effective electrocatalyst. However, perovskites in those studies were obtained from different synthesis techniques [12–14]. This deviation suggests that the superior performance of the LFO-based electrode may be attributed first, to the distinctive intrinsic properties of the spray-flame synthesized material that provides only minute amounts of organic residuals at the surface, and second, advanced electrode engineering that enables comparable anodes with only slight variations in the electrode microstructure, which have not been reported before. Although the LMO-based electrodes exhibited substantially higher overpotential, making it less promising, it will still be examined further under application-relevant conditions for a more comprehensive assessment of its capabilities.

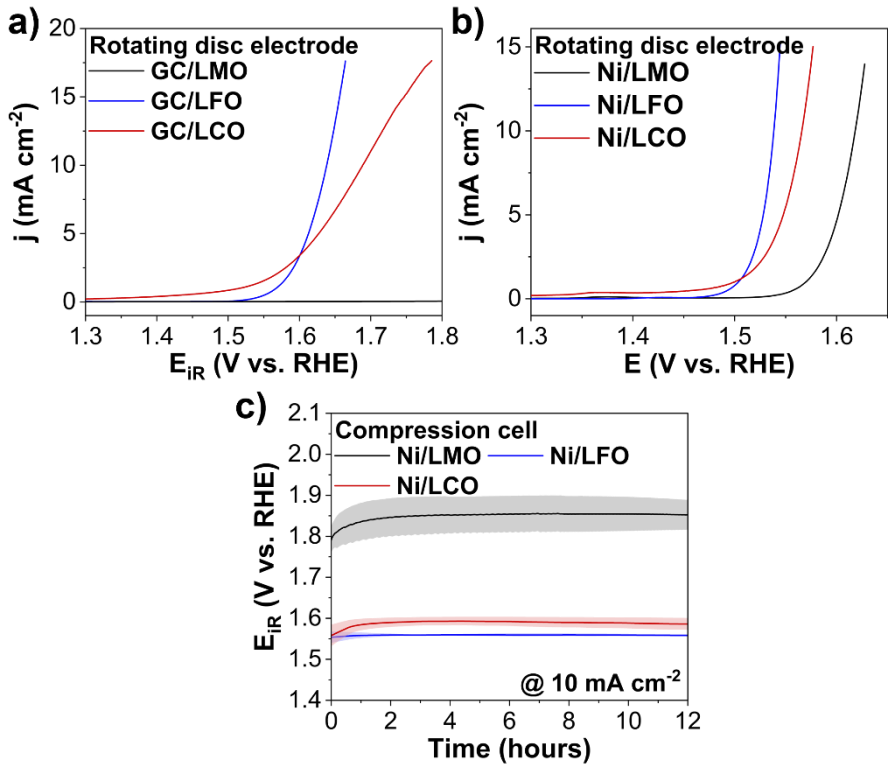

Figure 5. LSV curves of LMO- (black), LFO- (blue), and LCO-based electrodes (red) with Sustainion® obtained with the RDE (1600 rpm, O_2-saturated, purified 1 mol L^{-1} KOH) on glassy-carbon and nickel substrate (a, b). The shift to lower overpotentials is connected to material conductivity. CP measurements were recorded with the compression cell in a purified, O_2-saturated, 1 mol L^{-1} KOH. The solid lines correspond to the mean values, and the shadows represent their standard deviations (c).

3.4.3. Zero-gap full-cell test

Next, anode-testing based on the coherent workflow transitions to the scalable zero-gap full-cell setup (supplementary material, Figure S36) with membrane electrode assembly (MEA), making a significant step toward industrial applicability. In our previous study, we highlighted that polarization curves (equivalent to the LSV curves in the half-cell) and long-term stabilities at high current densities are key indicators of whether the combination of catalytic material, binder, and substrate is suitable for future development toward real-life applications [19,89].

Two trends are noticed in the polarization curves. The first one at 0.5 A cm^{-2} indicates that the polarization curves (Table 1, supplementary material, Figure S37a–d) mainly follow the trend noticed with the electrochemical standard laboratory half-cell electrochemical setups. The most significant difference is detected in polarization curves obtained after 36 h of electrochemical testing, where the LCO-based electrodes, for the first time, outperform LFO-based electrodes (supplementary material, Figure S37d). Second, the polarization curves of the LMO-based electrodes are much closer to the LCO- and LFO-based electrodes, indicating that the LMO-based anodes under application-relevant conditions show enhanced performance compared to the results gained at 10 mA cm^{-2}. Long-term stability CP measurements (Figure 6) were obtained at a current density of 0.5 A cm^{-2} for 12 h at room temperature and additionally for 24 h at 60 °C. After exposure for 12 h at room temperature, the cell potential (U_{cell}) of LMO- (2.32 V) and LCO-based electrodes (2.20 V) is relatively stable. In contrast, in the case of LFO-based electrodes (2.17 V), a significant increase in the potential is recorded. This further confirms that the overpotential of LMO-based electrodes during application-relevant conditions is significantly closer to the other two electrocatalysts than suggested by electrochemical half-cell testing.

Furthermore, to simulate real-life electrolyzer conditions more accurately, additional full-cell tests were conducted at 60 °C. In all cases, the elevated temperature led to a significant improvement in U_{cell}. The most substantial decrease in U_{cell} is observed with LMO-based electrodes (0.28 V) compared to the U_{cell} after testing at room temperature, followed by LFO- and LCO-based electrodes with 0.24 and 0.22 V, respectively. Similarly to room temperature measurements, the LFO-based electrodes again show the highest increase of the U_{cell} with time (0.15 V), followed by LMO- (0.12 V) and LCO-based electrodes (0.09 V), aligning with the trends observed in the polarization curves. After 36 h exposure, the LCO-based electrodes show lower U_{cell} compared to LFO- and LMO-based electrodes (2.07, 2.09, and 2.16 V).

This leads to a couple of conclusions. Firstly, all three perovskite electrocatalysts show promising performance for OER under application-relevant conditions. This includes the LMO-based electrodes, which would typically be discarded after the lab-testing conditions. Secondly, after 36 h, all electrocatalysts reach a plateau, indicating a steady state of the system. Thirdly, the curve-crossing trends observed between LFO- and LCO-based electrodes point towards material changes that are only evident under harsh conditions and are unknown to standard laboratory electrochemical testing. These changes will be investigated in the post-mortem analysis section.

Table 2. Electrochemical results on the three perovskites gained by electrochemical half-cell-testing at 10 mA cm^{-2} in purified, O_2-saturated, 1 mol L^{-1} KOH and results gained under application-relevant conditions with the zero-gap full-cell at 0.5 A cm^{-2} in as-prepared 1 mol L^{-1} KOH at room temperature and 60 °C.

	LMO / V vs. RHE	LFO / V vs. RHE	LCO / V vs. RHE
SDC / 10 mA cm^{-2}	1.635 ± 0.007	1.541 ± 0.002	1.560 ± 0.003
RDE/GC / 10 mA cm^{-2}	/	1.64	1.69
RDE/Ni / 10 mA cm^{-2}	1.62	1.54	1.57
Compression cell / 10 mA cm^{-2}	1.731 ± 0.007	1.54 ± 0.01	1.566 ± 0.004
	voltage / V	voltage / V	voltage / V
Zero-gap full-cell before CP at room temperature / 0.5 A cm^{-2}	2.27 ± 0.05	1.96 ± 0.09	2.14 ± 0.01
Zero-gap full-cell after CP at room temperature / 0.5 A cm^{-2}	2.23 ± 0.04	2.04 ± 0.03	2.15 ± 0.02
Zero-gap full-cell before CP at 60 °C / 0.5 A cm^{-2}	2.00 ± 0.03	1.86 ± 0.02	1.94 ± 0.05
Zero-gap full-cell after CP at 60 °C / 0.5 A cm^{-2}	2.08 ± 0.05	2.018 ± 0.002	1.97 ± 0.05

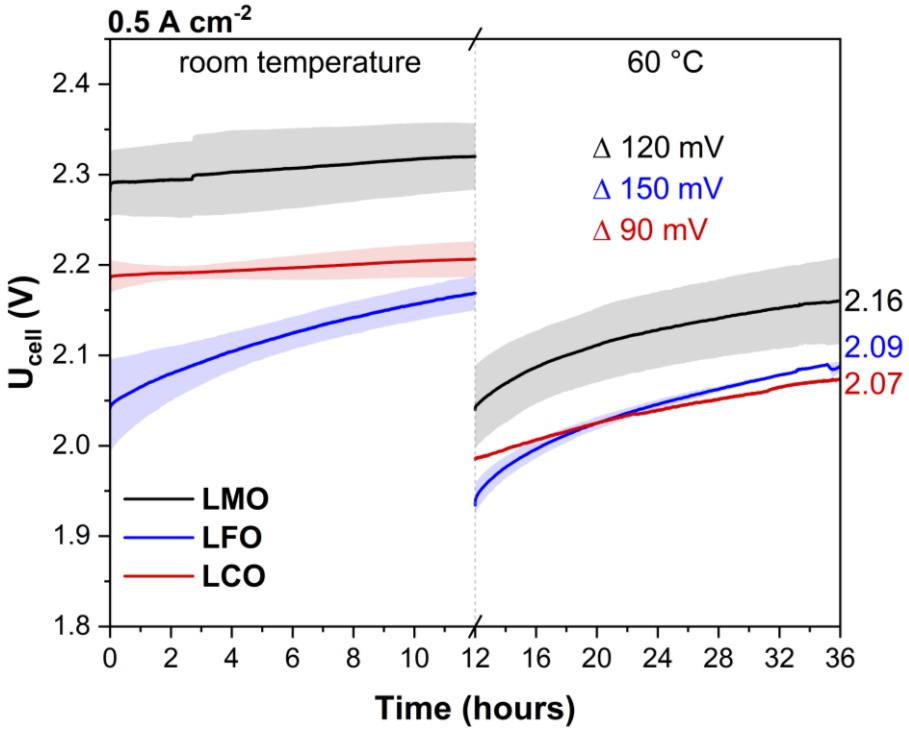

Figure 6. Zero-gap full-cell characterization of LMO- (black), LFO- (blue), and LCO-based electrodes (red) at room temperature and 60 °C at 0.5 A cm^{-2} in as-prepared 1 mol L^{-1} KOH on Ni foam substrates.

3.5. Post-mortem full-cell analysis

To gain a deeper understanding of performance changes, post-mortem analysis of the anodes after full-cell testing at room temperature and 60 °C was conducted using Raman spectroscopy, XPS, and GIXRD. These results were compared to pristine electrodes (Pristine) that were not exposed to electrochemical conditions. This enables us to understand catalytic mechanisms and provides, together with the electrochemical data, a comprehensive understanding of the materials' behavior under real-life operating conditions.

3.5.1. Post-mortem analysis of the thin films by Raman spectroscopy

Raman spectroscopy of all the LMO-based electrodes (Figure 7a–c) reveals two vibrational modes at 498 and 616 cm^{-1}, corresponding to Jahn-Teller distortion in the MnO_6 octahedra [39,40]. The full-cell testing at room temperature of the LMO-based electrode exhibits no significant differences from the pristine-LMO-based electrode before electrochemical testing. However, an additional Raman mode at 572 cm^{-1} is observed after full-cell testing at 60 °C. This is attributed to the Mn−O stretching vibration, indicating an increased presence of Mn^{4+} [90,91]. For LFO-based electrodes, a Raman mode at 642 cm^{-1} is detected in both the pristine-LFO-based electrode and LFO-based electrode after full-cell testing, corresponding to the FeO_6 octahedral stretching vibrations [41,43]. However, after full-cell testing at 60 °C, new Raman modes appear at 572 and 666 cm^{-1}, indicating an increased presence of Fe^{3+} due to surface changes most likely caused by chemical leaching under harsh conditions [92,93]. The leaching and deposition of iron on the surface align well with the ICP-OES data described above (electrochemical flow cell coupled with ICP-OES), where traces of iron were detected. On the other hand, lanthanum showed no dissolution.

These changes were additionally confirmed by EDX mapping of the LFO-based electrode after full-cell testing at 60 °C (supplementary material, Figure S38, Table S4), which revealed localized areas of increased iron concentration. In the case of LCO-based electrodes, the pristine-LCO-based electrode exhibits a Raman mode at 642 cm^{-1}, corresponding to the Co−O stretching vibrations [44,45]. After electrochemical exposure at 0.5 A cm^{-2}, a significant shift of 49 cm^{-1} is observed. The peak at 593 cm^{-1} in the LCO-based electrode after full-cell testing at room temperature and 60 °C is associated with the Co−O vibrations and formation of amorphous $CoO_x(OH)_y$. Additionally, the exposed shoulder is related to the Co−O−Co vibrations [94]. Moreover, TEM (supplementary material, Figure S39) was used to confirm the formation of an amorphous structure with a coexistence of crystalline and amorphous phases. The amorphization and catalytic mechanism were further validated using CV taken from the

compression cell (supplementary material, Figure S40) [95,96]. Notable changes between the 1st and 10th or 50th cycle suggest that the LCO-based electrode underwent irreversible conversion from Co(II) to Co(III), which can be related to the formation of $CoO_x(OH)_y$ on the surface [86,97]. This is in line with findings from Li et al. [98] who demonstrated that the amorphization process of LCO improves the activity of the electrocatalyst, which may explain the significantly improved stability of LCO-based electrodes at 0.5 A cm^{-2} in comparison to LFO- and LMO-based electrodes. Similar studies by Cai et al. [99] and Indra et al. [100] also support the observation that amorphous catalysts exhibit superior activity and stability compared to crystalline structures.

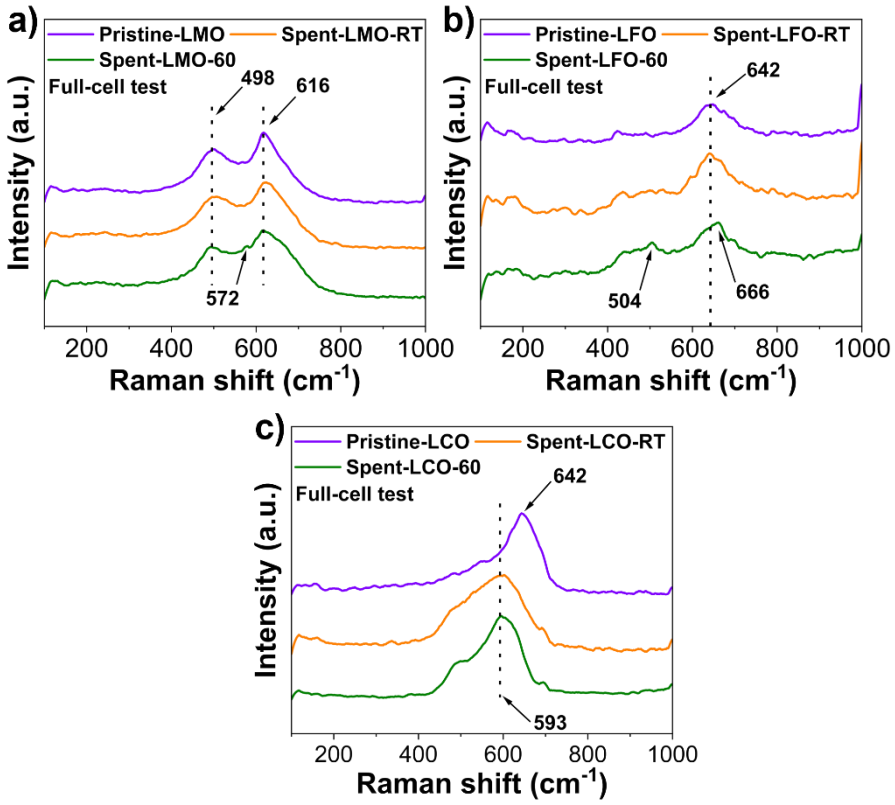

Figure 7. Raman spectroscopy data of LMO-, LFO-, and LCO-based electrodes (a, b, and c) before and after electrochemical testing in a zero-gap full-cell. Measurements were performed on pristine electrodes (magenta) and electrodes after full-cell testing at room temperature (spent-RT, orange) and 60 °C (spent-60, green).

3.5.2. Post-mortem XPS analysis of the thin films

XPS analysis of the LMO-based electrodes (Figure 8a-b, supplementary material, Figure S41a) reveals that the La $3d_{5/2}$ spectra for the pristine-LMO sample and electrodes after full-cell testing at room temperature and 60 °C exhibit a multiplet peak split difference of 3.7 eV, characteristic of La-based perovskites [46,47]. The Mn $2p_{3/2}$ spectra after full-cell testing at room temperature and 60 °C show a shift from 641.6 to 642.1 eV toward higher binding energies. This shift is associated with an increased presence of Mn^{4+}, which aligns well with the Raman data [101,102]. Additionally, O 1s spectra across all samples indicate a reduction in $O_{lattice}$ and an increase in surface oxygen species [103]. For the LFO-based electrode, a slight narrowing of the La $3d_{5/2}$ multiplet distance is detected, decreasing from 3.8 eV in the pristine-LFO sample to 3.6 eV after full-cell testing at 60 °C (supplementary material, Figure S41b). However, this value remains near the literature-reported 3.7 eV [46,47]. The Fe $2p_{3/2}$ demonstrates a significant change in the LFO-based electrode after full-cell testing at 60 °C compared to the other two LFO samples, as the peak emerges at 713.7 eV, which is associated with the increasing presence of Fe^{3+} on the surface (Figure 8c) [101,102]. Similar to the case of LMO-based electrodes, O 1s spectra of LFO-based samples suggest a rise in adsorbed oxygen species and a decrease in $O_{lattice}$ on the surface after electrochemical evaluation (Figure 8d). For LCO-based samples, the La $3d_{5/2}$ multiplet distance (supplementary material, Figure S41c) is reduced from 3.8 to 3.5 eV, indicating the formation of $La(OH)_3$ on the electrode surface during OER [96]. This formation on the surface was also observed by Bai et al. [96], who suggested that this is the main reason for the amorphization of LCO material. The Co $2p_{3/2}$ after full-cell testing at 60 °C (Figure 8e) displays an increase in Co^{3+}, as evidenced by a slight shift towards lower binding energies from 782.2 to 781.7 eV. This confirms the formation of a $CoO_x(OH)_y$ [96,97]. Meanwhile, O 1s spectra (Figure 8f) indicate an increase of adsorbed oxygen species on the surface and a decrease of metal oxides originating from the bulk, which is expected during water electrolysis. In general, XPS and Raman spectroscopy data show excellent agreement and

correlate very well with the electrochemical data, which makes them ideal complementary techniques for future post-mortem analysis.

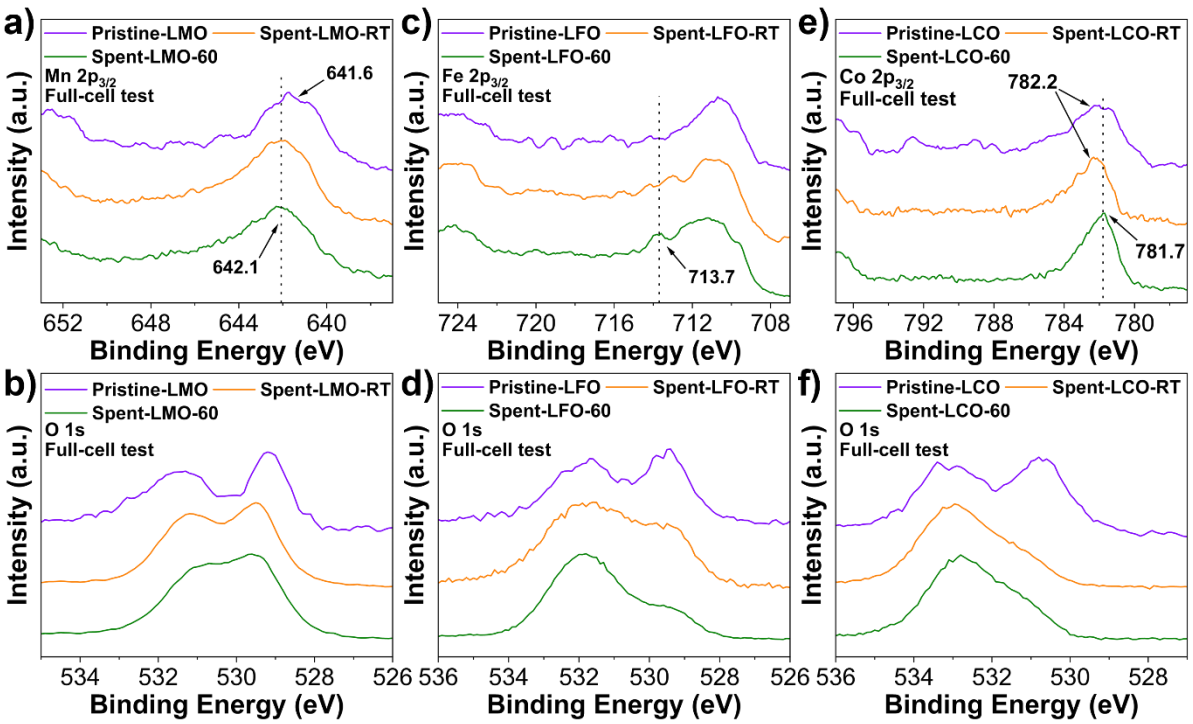

Figure 8. XPS data of Mn $2p_{3/2}$ and O1s on LMO-based electrodes (a, b). XPS data of Fe $2p_{3/2}$ and O1s on LFO-based electrodes (c, d). XPS data of Co $2p_{3/2}$ and O1s on LCO-based electrodes (e, f). Measurements are performed on pristine perovskite electrodes (magenta) and electrodes after full-cell testing at room temperature (spent-RT, orange) and at 60 °C (spent-60, green). All materials were exposed to a current density of 0.5 A cm^{-2}.

3.5.3. Post-mortem GIXRD analysis of the thin films

Additionally, GIXRD was performed on all three perovskite-based electrodes. As shown in Figure S42a–c (supplementary material), the nickel substrate dominates the diffraction patterns, with distinct peaks at 2θ = 44.5° and 52.9°. These correspond to the nickel foam and its non-flat nature. As a result, some of the catalytic material spills around the edges, leading to thinner material deposits on the surface and exposing more of the nickel substrate. In all cases, a gentle peak is visible in the area between 2θ = 32° and 33°, which is connected to the perovskite

structure. However, a closer examination reveals that LMO- and LFO-based electrodes after full-cell testing at room temperature and 60 °C exhibit no structural changes after exposure to harsh conditions, suggesting that these materials maintain robust structural integrity. However, in LCO-based electrodes, a peak shift after full-cell testing at 60 °C is detected towards lower 2θ values, which indicates the anodes' deformation in a crystalline structure. This observation aligns with the findings from Raman and XPS analysis. However, due to intense nickel peaks, a more detailed determination of the crystalline structure of LCO is not possible. Nonetheless, this shift indicates the presence of a mixture of phases within the LCO material.

In total, the combined results from post-mortem analyses, using Raman spectroscopy, XPS, and GIXRD, after electrochemical half-cell and full-cell testing reveal a direct link between the material's electrochemical performance and the observed materials properties. Notably, full-cell testing provides insights into the materials' behavior under realistic operating conditions that are not accessible through half-cell experiments alone. This integrated approach underscores the importance of evaluating electrode stability and reactivity at high current densities.

4. Conclusions

In this research, we investigated the effects of electrode material engineering on OER performance and emphasized the importance of the integration of scalable technologies and application-relevant testing into the material exploration process. By incorporating a structured, coherent workflow, we demonstrated a comprehensive strategy to evaluate La-based perovskites at different scales. This approach also accelerates knowledge transfer for the future development of next-generation electrocatalysts on relevant scales that are crucial to alleviating climate change. Based on our investigation, we can conclude:

- Firstly, perovskite nanopowders synthesized using spray-flame synthesis are highly crystalline, phase-pure materials with huge specific surface areas above 80 $m^2 g^{-1}$. Their

unique intrinsic properties provide a strong foundation for larger-scale catalyst production.

- Secondly, dispersion stability and ink formulation were proven as crucial factors for efficient and reproducible electrode preparation. All three nanomaterials demonstrate good dispersibility in ethanol. However, the dispersion stability decreases with increasing water-content in the continuous phase. Stability problems can be overcome by the incorporation of Sustainion® XA-9 binder, which significantly improves ink stability and presents an important step towards a fluorine-free technology (per- and poly-fluoroalkyl substances – PFAS).
- Thirdly, morphological electrode evaluation revealed a correlation between the particle size after synthesis and the surface roughness of the electrodes, with LCO-based anodes exhibiting the highest roughness and porosity, which is connected to improved bubble management and exposure to active sites. Furthermore, coating homogeneity assessed using SDC shows low standard deviations, no delamination, and better OER performance of LFO-based anodes compared to the LCO-based material as reported in the literature [12–14,16].
- Fourthly, electrochemical testing, including compression cell and RDE analysis, supports the SDC results and gives the first indications about the superior electrochemical performance of LFO- compared to LCO- and LMO-based electrodes. As the most important, all perovskites presented robust properties under laboratory testing conditions, which made them suitable candidates for further studies under real-life conditions in a zero-gap full-cell. Notably, full-cell testing at 60 °C revealed a change in OER performance due to a significant increase in the potential of the LFO-based sample, leading to a polarization-curve-crossing with the LCO-based electrode. Moreover, the LMO-based anode presents enhanced performance at high current

densities compared to 10 mA cm^{-2}, indicating its potential as a toxic-metal-free OER electrocatalyst.

- Finally, we could strengthen the electrochemical observations with post-mortem analysis using Raman spectroscopy, XPS, and GIXRD, which enables investigations of materials stability and catalytic mechanisms. Changes in LMO-based anodes were linked to the increasing presence of Mn^{4+}, while LFO degradation correlated with iron leaching and increased Fe^{3+} concentration on the anode surface. In contrast, LCO-based anodes underwent structural changes connected to amorphization, resulting in enhanced long-term electrochemical stability.

Altogether, our findings contribute to the systematic exploration of perovskite-based OER electrocatalysts, where the faster integration of full-cell testing into the materials' assessment enhances our understanding of electrocatalyst behavior. We believe that these studies are needed to holistically understand electrocatalysts and enable bridging the gap between academia and industry. Notably, our results highlight the potential of gas-phase-synthesized perovskites using non-toxic, earth-abundant transitional metals such as iron and manganese. However, as presented, further development of electrocatalytic material stability and a deeper understanding of the substrate effect on OER performance are needed to complete the whole picture of the effective electrode production for alkaline water electrolysis.

Declaration of competing interest

All authors declare no conflict of interest.

Acknowledgments

B. Toplak gratefully acknowledges a scholarship from the International Max Planck Research School (IMPRS) RECHARGE doctoral program. A.R. Khan acknowledges the support of a Ph.D. fellowship awarded by the Higher Education Commission (HEC) of Pakistan and the German Academic Exchange Service (DAAD). K. Yahuza Muhammad. acknowledges Petroleum Technology Development Fund (PTDF), Nigeria for doctoral fellowship with Pef No.: PTDF/ED/OSS/PHD/KYM/1723/20 and ID: 20PHD031.The authors acknowledge funding by the German Research Foundation (DFG) within the CRC/TRR 247 (Heterogeneous Oxidation Catalysis in the Liquid Phase 388390466), the Mercator Research Center Ruhr within the DIMENSION project (MERCUR.Exzellenz, 'DIMENSION' Ex-2021-0034). D. Segets, H. Hoster, C. Schulz, C. Andronescu, and U.-P. Apfel would also like to acknowledge the Ministry of Culture and Science of the State of North Rhine-Westphalia (Materials for Future Hydrogen Technologies – Mat4Hy) support. All contributors acknowledge MAT4HY.NRW Consortium for cooperative support. C. Andronescu acknowledges funding by the Ministry of Culture and Science of the State of North Rhine-Westphalia (PB NRW 2022 - Application 19). The authors also gratefully acknowledge the support from the Interdisciplinary Center for Analytics on the Nanoscale (ICAN), a core facility at the University of Duisburg-Essen. The nanopowder X-Ray data were collected using the Panalytical Empyrean at the Institute for Materials Science (UDEMAT). We would like to thank D.C. Lupascu for assistance in using the instrument. The electrode X-ray data were collected using the Rigaku Smartlab High-Resolution diffractometer of the Nanoparticle Processing Technology (NPPT) group at the University of Duisburg-Essen. The instrument is funded through the DFG Instrument proposal INST 20876/395-1 FUGG project number 450350889 and the state of North Rhine-Westphalia, Germany. We would like to thank M. Schroer for assistance in using the instrument.

Data Availability Statement

The data that support the findings of this study are openly available at Zenodo at 10.5281/zenodo.15348465.

References

[1] S. Anantharaj, S.R. Ede, K. Sakthikumar, K. Karthick, S. Mishra, S. Kundu, Recent Trends and Perspectives in Electrochemical Water Splitting with an Emphasis on Sulfide, Selenide, and Phosphide Catalysts of Fe, Co, and Ni: A Review, ACS Catal. 6 (2016) 8069–8097. https://doi.org/10.1021/acscatal.6b02479.

[2] B. Mohanty, P. Bhanja, B.K. Jena, An overview on advances in design and development of materials for electrochemical generation of hydrogen and oxygen, Materials Today Energy 23 (2022) 100902. https://doi.org/10.1016/j.mtener.2021.100902.

[3] J.X. Flores-Lasluisa, F. Huerta, D. Cazorla-Amorós, E. Morallón, LaNi1-xCoxO3 perovskites for application in electrochemical reactions involving molecular oxygen, Energy 273 (2023) 127256. https://doi.org/10.1016/j.energy.2023.127256.

[4] A. Ashok, A. Kumar, J. Ponraj, S.A. Mansour, F. Tarlochan, Enhancing the electrocatalytic properties of LaMnO3 by tuning surface oxygen deficiency through salt assisted combustion synthesis, Catalysis Today 375 (2021) 484–493. https://doi.org/10.1016/j.cattod.2020.05.065.

[5] M.S. Alom, C.C.W. Kananke-Gamage, F. Ramezanipour, Perovskite Oxides as Electrocatalysts for Hydrogen Evolution Reaction, ACS Omega 7 (2022) 7444–7451. https://doi.org/10.1021/acsomega.1c07203.

[6] J. Suntivich, K.J. May, H.A. Gasteiger, J.B. Goodenough, Y. Shao-Horn, A perovskite oxide optimized for oxygen evolution catalysis from molecular orbital principles, Science 334 (2011) 1383–1385. https://doi.org/10.1126/science.1212858.

[7] J.A. Dias, M.A.S. Andrade, H.L.S. Santos, M.R. Morelli, L.H. Mascaro, Lanthanum-Based Perovskites for Catalytic Oxygen Evolution Reaction, ChemElectroChem 7 (2020) 3173–3192. https://doi.org/10.1002/celc.202000451.

[8] A. Mendoza, O. Guzmán, Low-Doped Regime Experiments in LaMnO 3 Perovskites by Simultaneous Substitution on Both La and Mn Sites, in: P. Sharma, A. Kumar (Eds.), Recent Advances in Multifunctional Perovskite Materials, IntechOpen, 2022.

[9] J. Chen, M. Shen, X. Wang, G. Qi, J. Wang, W. Li, The influence of nonstoichiometry on LaMnO3 perovskite for catalytic NO oxidation, Applied Catalysis B: Environmental 134-135 (2013) 251–257. https://doi.org/10.1016/j.apcatb.2013.01.027.

[10] Z. Jia, C. Cheng, X. Chen, L. Liu, R. Ding, J. Ye, J. Wang, L. Fu, Y. Cheng, Y. Wu, Applications of all-inorganic perovskites for energy storage, Mater. Adv. 4 (2023) 79–104. https://doi.org/10.1039/D2MA00779G.

[11] Y. Wang, Y. Wang, X. Liu, Y. Guo, Y. Guo, G. Lu, Nanocasted synthesis of the mesostructured LaCoO3 perovskite and its catalytic activity in methane combustion, J. Nanosci. Nanotechnol. 9 (2009) 933–936. https://doi.org/10.1166/jnn.2009.c057.

[12] A. Ashok, A. Kumar, R.R. Bhosale, F. Almomani, S.S. Malik, S. Suslov, F. Tarlochan, Combustion synthesis of bifunctional LaMO3 (M = Cr, Mn, Fe, Co, Ni) perovskites for oxygen reduction and oxygen evolution reaction in alkaline media, Journal of

Electroanalytical Chemistry 809 (2018) 22–30. https://doi.org/10.1016/j.jelechem.2017.12.043.
[13] M.V. Kante, M.L. Weber, S. Ni, I.C.G. van den Bosch, E. van der Minne, L. Heymann, L.J. Falling, N. Gauquelin, M. Tsvetanova, D.M. Cunha, G. Koster, F. Gunkel, S. Nemšák, H. Hahn, L. Velasco Estrada, C. Baeumer, A High-Entropy Oxide as High-Activity Electrocatalyst for Water Oxidation, ACS Nano 17 (2023) 5329–5339. https://doi.org/10.1021/acsnano.2c08096.
[14] T.X. Nguyen, Y.-C. Liao, C.-C. Lin, Y.-H. Su, J.-M. Ting, 2021. Advanced High Entropy Perovskite Oxide Electrocatalyst for Oxygen Evolution Reaction. Adv Funct Materials 31, 2101632. https://doi.org/10.1002/adfm.202101632.
[15] R. Xie, Z. Nie, X. Hu, Y. Yu, C. Aruta, N. Yang, Pr-Doped LaCoO 3 toward Stable and Efficient Oxygen Evolution Reaction, ACS Appl. Energy Mater. 4 (2021) 9057–9065. https://doi.org/10.1021/acsaem.1c01348.
[16] J.X. Flores-Lasluisa, F. Huerta, D. Cazorla-Amorós, E. Morallon, Carbon Material and Cobalt-Substitution Effects in the Electrochemical Behavior of LaMnO3 for ORR and OER, Nanomaterials (Basel) 10 (2020). https://doi.org/10.3390/nano10122394.
[17] M.M. Rashad, E.M. Elsayed, M.M. Moharam, R.M. Abou-Shahba, A.E. Saba, Structure and magnetic properties of NixZn1−xFe2O4 nanoparticles prepared through co-precipitation method, Journal of Alloys and Compounds 486 (2009) 759–767. https://doi.org/10.1016/j.jallcom.2009.07.051.
[18] F. Li, J. Ran, M. Jaroniec, S.Z. Qiao, Solution combustion synthesis of metal oxide nanomaterials for energy storage and conversion, Nanoscale 7 (2015) 17590–17610. https://doi.org/10.1039/c5nr05299h.
[19] P. Gerschel, S. Angel, M. Hammad, A. Olean-Oliveira, B. Toplak, V. Chanda, R. Martínez-Hincapié, S. Sanden, A.R. Khan, Da Xing, A.S. Amin, H. Wiggers, H. Hoster, V. Čolić, C. Andronescu, C. Schulz, U.-P. Apfel, D. Segets, 2024. Determining materials for energy conversion across scales: The alkaline oxygen evolution reaction. Carbon Energy, e608. https://doi.org/10.1002/cey2.608.
[20] M. Hammad, S. Angel, A.K. Al-Kamal, A. Asghar, M.-A. Kräenbring, A. Amin, H.T. Wiedemann, A.S. Amin, V. Vinayakumar, T.C. Schmidt, C.W. Kay, D. Segets, H. Wiggers, Spray-flame synthesis of LaCo0.2Mn0.8O3 for selective peroxymonosulfate activation into singlet oxygen towards efficient degradation of carbamazepine, Process Safety and Environmental Protection 194 (2025) 1347–1359. https://doi.org/10.1016/j.psep.2024.12.060.
[21] S. Angel, J.D. Tapia, J. Gallego, U. Hagemann, H. Wiggers, Spray-Flame Synthesis of LaMnO 3+δ Nanoparticles for Selective CO Oxidation (SELOX), Energy Fuels 35 (2021) 4367–4376. https://doi.org/10.1021/acs.energyfuels.0c03659.
[22] L. Grebener, A.S. Odungat, Y. Zhu, O. Pasdag, I. Radev, E. Nürenberg, A. Kubina, V. Peinecke, S. Kohsakowski, D. Segets, F. Özcan, Investigation of fuel cell catalyst dispersion formulations for indirect roll-to-roll fabrication of catalyst coated membranes for proton exchange membrane fuel cells, Journal of Power Sources 635 (2025) 236457. https://doi.org/10.1016/j.jpowsour.2025.236457.
[23] A. Jain, C. Marcks, L. Grebener, J. Johny, A.S. Odungat, M. Chatwani, M.-A. Kräenbring, A. Shaji, M.F. Tesch, A.K. Mechler, V. Vinayakumar, D. Segets, 2025. A Proof-of-Principle Demonstration: Exploring the Effect of Anode Layer Microstructure on the Alkaline Oxygen Evolution Reaction. Adv Funct Materials, 2421352. https://doi.org/10.1002/adfm.202421352.

[24] F. Schneider, S. Suleiman, J. Menser, E. Borukhovich, I. Wlokas, A. Kempf, H. Wiggers, C. Schulz, SpraySyn-A standardized burner configuration for nanoparticle synthesis in spray flames, Rev. Sci. Instrum. 90 (2019) 85108. https://doi.org/10.1063/1.5090232.
[25] C. Schulz, T. Dreier, M. Fikri, H. Wiggers, Gas-phase synthesis of functional nanomaterials: Challenges to kinetics, diagnostics, and process development, Proceedings of the Combustion Institute 37 (2019) 83–108. https://doi.org/10.1016/j.proci.2018.06.231.
[26] S. Hardt, I. Wlokas, C. Schulz, H. Wiggers, Impact of Ambient Pressure on Titania Nanoparticle Formation During Spray-Flame Synthesis, J. Nanosci. Nanotechnol. 15 (2015) 9449–9456. https://doi.org/10.1166/jnn.2015.10607.
[27] S. Bapat, C. Giehl, S. Kohsakowski, V. Peinecke, M. Schäffler, D. Segets, On the state and stability of fuel cell catalyst inks, Advanced Powder Technology 32 (2021) 3845–3859. https://doi.org/10.1016/j.apt.2021.08.030.
[28] O. Anwar, A.S. Amin, A. Amin, M.-A. Kräenbring, F. Özcan, D. Segets, 2023. Determination of Hansen Parameters of Nanoparticles: A Comparison of Two Methods Using Titania, Carbon Black, and Silicon/Carbon Composite Materials. Part & Part Syst Charact 40, 2300050. https://doi.org/10.1002/ppsc.202300050.
[29] S. Süß, T. Sobisch, W. Peukert, D. Lerche, D. Segets, Determination of Hansen parameters for particles: A standardized routine based on analytical centrifugation, Advanced Powder Technology 29 (2018) 1550–1561. https://doi.org/10.1016/j.apt.2018.03.018.
[30] R. Martínez-Hincapié, J. Wegner, M.U. Anwar, A. Raza-Khan, S. Franzka, S. Kleszczynski, V. Čolić, The determination of the electrochemically active surface area and its effects on the electrocatalytic properties of structured nickel electrodes produced by additive manufacturing, Electrochimica Acta 476 (2024) 143663. https://doi.org/10.1016/j.electacta.2023.143663.
[31] V. Chanda, D. Blaudszun, L. Hoof, I. Sanjuán, K. Pellumbi, K. junge Puring, C. Andronescu, U.-P. Apfel, 2024. Exploring the (Dis)-Similarities of Half-Cell and Full Cell Zero-Gap Electrolyzers for the CO 2 Electroreduction. ChemElectroChem 11, e202300715. https://doi.org/10.1002/celc.202300715.
[32] A. Loh, X. Li, S. Sluijter, P. Shirvanian, Q. Lai, Y. Liang, Design and Scale-Up of Zero-Gap AEM Water Electrolysers for Hydrogen Production, Hydrogen 4 (2023) 257–271. https://doi.org/10.3390/hydrogen4020018.
[33] M. Pidburtnyi, B. Zanca, C. Coppex, S. Jimenez-Villegas, V. Thangadurai, A Review on Perovskite-Type LaFeO 3 Based Electrodes for CO 2 Reduction in Solid Oxide Electrolysis Cells: Current Understanding of Structure–Functional Property Relationships, Chem. Mater. 33 (2021) 4249–4268. https://doi.org/10.1021/acs.chemmater.1c00771.
[34] Z. Shen, Y. Zhuang, W. Li, X. Huang, F.E. Oropeza, E.J.M. Hensen, J.P. Hofmann, M. Cui, A. Tadich, D. Qi, J. Cheng, J. Li, K.H.L. Zhang, Increased activity in the oxygen evolution reaction by Fe 4+ -induced hole states in perovskite La 1−x Sr x FeO 3, J. Mater. Chem. A 8 (2020) 4407–4415. https://doi.org/10.1039/C9TA13313E.
[35] Y. Zhu, W. Zhou, J. Yu, Y. Chen, M. Liu, Z. Shao, Enhancing Electrocatalytic Activity of Perovskite Oxides by Tuning Cation Deficiency for Oxygen Reduction and Evolution Reactions, Chem. Mater. 28 (2016) 1691–1697. https://doi.org/10.1021/acs.chemmater.5b04457.
[36] Y.D. Susanti, N. Afifah, R. Saleh, Ag modified LaMnO 3 nanoparticles for methylene blue degradation via photosonocatalytic activities, IOP Conf. Ser.: Mater. Sci. Eng. 496 (2019) 12037. https://doi.org/10.1088/1757-899X/496/1/012037.

[37] S. Thirumalairajan, K. Girija, N.Y. Hebalkar, D. Mangalaraj, C. Viswanathan, N. Ponpandian, Shape evolution of perovskite LaFeO3 nanostructures: a systematic investigation of growth mechanism, properties and morphology dependent photocatalytic activities, RSC Adv. 3 (2013) 7549. https://doi.org/10.1039/c3ra00006k.
[38] S. Zhou, X. Miao, X. Zhao, C. Ma, Y. Qiu, Z. Hu, J. Zhao, L. Shi, J. Zeng, Engineering electrocatalytic activity in nanosized perovskite cobaltite through surface spin-state transition, Nat. Commun. 7 (2016) 11510. https://doi.org/10.1038/ncomms11510.
[39] M.N. Iliev, M.V. Abrashev, H.-G. Lee, V.N. Popov, Y.Y. Sun, C. Thomsen, R.L. Meng, C.W. Chu, Raman spectroscopy of orthorhombic perovskitelike YMnO3 and LaMnO3, Phys. Rev. B 57 (1998) 2872–2877. https://doi.org/10.1103/PhysRevB.57.2872.
[40] M.V. Abrashev, A.P. Litvinchuk, M.N. Iliev, R.L. Meng, V.N. Popov, V.G. Ivanov, R.A. Chakalov, C. Thomsen, Comparative study of optical phonons in the rhombohedrally distorted perovskites LaAlO3 and LaMnO3, Phys. Rev. B 59 (1999) 4146–4153. https://doi.org/10.1103/PhysRevB.59.4146.
[41] A.F. Manchón-Gordón, P.E. Sánchez-Jiménez, J.S. Blázquez, A. Perejón, L.A. Pérez-Maqueda, Structural, Vibrational, and Magnetic Characterization of Orthoferrite LaFeO3 Ceramic Prepared by Reaction Flash Sintering, Materials (Basel) 16 (2023). https://doi.org/10.3390/ma16031019.
[42] Y. Huang, J. Liu, D. Cao, Z. Liu, K. Ren, K. Liu, A. Tang, Z. Wang, L. Li, S. Qu, Z. Wang, Separation of hot electrons and holes in Au/LaFeO3 to boost the photocatalytic activities both for water reduction and oxidation, International Journal of Hydrogen Energy 44 (2019) 13242–13252. https://doi.org/10.1016/j.ijhydene.2019.03.182.
[43] M. Połomska, B. Hilczer, J. Wolak, A. Pietraszko, M. Balcerzak, M. Jurczyk, J. Jakubowicz, XRD and Raman spectroscopy studies of (Bi 1– x La x FeO 3) 0.5 (PbTiO 3) 0.5 solid solution, Phase Transitions 87 (2014) 909–921. https://doi.org/10.1080/01411594.2014.953519.
[44] L. Tepech-Carrillo, A. Escobedo-Morales, A. Pérez-Centeno, E. Chigo-Anota, J.F. Sánchez-Ramírez, E. López-Apreza, J. Gutiérrez-Gutiérrez, Preparation of Nanosized LaCoO 3 through Calcination of a Hydrothermally Synthesized Precursor, Journal of Nanomaterials 2016 (2016) 1–7. https://doi.org/10.1155/2016/6917950.
[45] Y.-P. Zhang, H.-F. Liu, H.-L. Hu, R.-S. Xie, G.-H. Ma, J.-C. Huo, H.-B. Wang, Orientation-dependent structural and photocatalytic properties of LaCoO3 epitaxial nano-thin films, R. Soc. Open Sci. 5 (2018) 171376. https://doi.org/10.1098/rsos.171376.
[46] H.A. Martinez-Rodriguez, K. Onyekachi, A. Concha-Balderrama, G. Herrera-Pérez, J.A. Matutes-Aquino, J.F. Jurado, M.H. Bocanegra-Bernal, V.-H. Ramos-Sánchez, J.A. Duarte-Moller, A. Reyes-Rojas, Electronic configuration and magnetic properties of La0.7Ca0.3Mn1-xFexO3 perovskite NPs: The effect of a lower Fe3+ concentration, Journal of Alloys and Compounds 816 (2020) 152668. https://doi.org/10.1016/j.jallcom.2019.152668.
[47] D. Çoban Özkan, A. Türk, E. Çelik, Synthesis and characterizations of sol–gel derived LaFeO3 perovskite powders, J Mater Sci: Mater Electron 31 (2020) 22789–22809. https://doi.org/10.1007/s10854-020-04803-8.
[48] J.X. Flores-Lasluisa, F. Huerta, D. Cazorla-Amorós, E. Morallón, Manganese oxides/LaMnO3 perovskite materials and their application in the oxygen reduction reaction, Energy 247 (2022) 123456. https://doi.org/10.1016/j.energy.2022.123456.
[49] G. Fang, K. Liu, M. Fan, J. Xian, Z. Wu, L. Wei, H. Tian, H. Jiang, W. Xu, H. Jin, J. Wan, Unveiling the electron configuration-dependent oxygen evolution activity of 2D porous

Sr-substituted LaFeO 3 perovskite through microwave shock, Carbon Neutralization 2 (2023) 709–720. https://doi.org/10.1002/cnl2.94.
[50] M. Wang, B. Han, J. Deng, Y. Jiang, M. Zhou, M. Lucero, Y. Wang, Y. Chen, Z. Yang, A.T. N'Diaye, Q. Wang, Z.J. Xu, Z. Feng, Influence of Fe Substitution into LaCoO3 Electrocatalysts on Oxygen-Reduction Activity, ACS Appl. Mater. Interfaces 11 (2019) 5682–5686. https://doi.org/10.1021/acsami.8b20780.
[51] M. Hammad, S. Angel, A.K. Al-Kamal, A. Asghar, A. Said Amin, M.-A. Kräenbring, H.T. Wiedemann, V. Vinayakumar, M. Yusuf Ali, P. Fortugno, C. Kim, T.C. Schmidt, C.W. Kay, C. Schulz, D. Segets, H. Wiggers, Synthesis of novel LaCoO3/graphene catalysts as highly efficient peroxymonosulfate activator for the degradation of organic pollutants, Chemical Engineering Journal 454 (2023) 139900. https://doi.org/10.1016/j.cej.2022.139900.
[52] J. Qian, T. Wang, Z. Zhang, Y. Liu, J. Li, D. Gao, Engineered spin state in Ce doped LaCoO3 with enhanced electrocatalytic activity for rechargeable Zn-Air batteries, Nano Energy 74 (2020) 104948. https://doi.org/10.1016/j.nanoen.2020.104948.
[53] Z. Li, L. Lv, J. Wang, X. Ao, Y. Ruan, D. Zha, G. Hong, Q. Wu, Y. Lan, C. Wang, J. Jiang, M. Liu, Engineering phosphorus-doped LaFeO3-δ perovskite oxide as robust bifunctional oxygen electrocatalysts in alkaline solutions, Nano Energy 47 (2018) 199–209. https://doi.org/10.1016/j.nanoen.2018.02.051.
[54] R. Wang, C. Ye, H. Wang, F. Jiang, Z-Scheme LaCoO3/g-C3N4 for Efficient Full-Spectrum Light-Simulated Solar Photocatalytic Hydrogen Generation, ACS Omega 5 (2020) 30373–30382. https://doi.org/10.1021/acsomega.0c03318.
[55] M. Khalifa, A.M. El Sayed, S.M. Kassem, E. Tarek, Synthesis, structural, optical, and thermal properties of LaFeO3/Poly(methyl methacrylate)/Poly(vinyl acetate) nanocomposites for radiation shielding, Sci. Rep. 14 (2024) 3672. https://doi.org/10.1038/s41598-024-54207-5.
[56] S. Abbot, Solubility Science: Principles and Practice, Creative Commons BY-ND, 2017.
[57] O. Anwar, S. Bapat, J. Ahmed, X. Xie, J. Sun, D. Segets, Hansen parameter evaluation for the characterization of titania photocatalysts using particle size distributions and combinatorics, Nanoscale 14 (2022) 13593–13607. https://doi.org/10.1039/d2nr02711a.
[58] A.S. Amin, D. Lerche, A.S. Odungat, S.U. Boehm, T. Koch, F. Özcan, D. Segets, 2024. A Procedure for Rational Probe Liquids Selection to Determine Hansen Solubility Parameters. ChemCatChem, e202301393. https://doi.org/10.1002/cctc.202301393.
[59] S. Bapat, D. Segets, Sedimentation Dynamics of Colloidal Formulations through Direct Visualization: Implications for Fuel Cell Catalyst Inks, ACS Appl. Nano Mater. 3 (2020) 7384–7391. https://doi.org/10.1021/acsanm.0c01467.
[60] S. Khandavalli, J.H. Park, N.N. Kariuki, D.J. Myers, J.J. Stickel, K. Hurst, K.C. Neyerlin, M. Ulsh, S.A. Mauger, Rheological Investigation on the Microstructure of Fuel Cell Catalyst Inks, ACS Appl. Mater. Interfaces 10 (2018) 43610–43622. https://doi.org/10.1021/acsami.8b15039.
[61] L. de Sousa, C. Harmoko, N. Benes, G. Mul, Optimizing the Ink Formulation for Preparation of Cu-Based Gas Diffusion Electrodes Yielding Ethylene in Electroreduction of CO 2, ACS EST Eng. 1 (2021) 1649–1658. https://doi.org/10.1021/acsestengg.1c00228.
[62] Z. Xu, J. Liang, L. Zhou, Photo-Fenton-like degradation of azo dye methyl orange using synthetic ammonium and hydronium jarosite, Journal of Alloys and Compounds 546 (2013) 112–118. https://doi.org/10.1016/j.jallcom.2012.08.087.
[63] H.J. Kim, S.H. Kim, S.-W. Kim, J.-K. Kim, C. Cao, Y. Kim, U. Kim, G. Lee, J.-Y. Choi, H.-S. Oh, H.-C. Song, W.J. Choi, H. Park, J.M. Baik, Low-temperature crystallization of

LaFeO3 perovskite with inherent catalytically surface for the enhanced oxygen evolution reaction, Nano Energy 105 (2023) 108003. https://doi.org/10.1016/j.nanoen.2022.108003.
[64] G. Mladin, M. Ciopec, A. Negrea, N. Duteanu, P. Negrea, P. Ianasi, C. Ianași, Silica- Iron Oxide Nanocomposite Enhanced with Porogen Agent Used for Arsenic Removal, Materials (Basel) 15 (2022). https://doi.org/10.3390/ma15155366.
[65] G.M. Estrada-Villegas, G. Morselli, M.J.A. Oliveira, G. González-Pérez, A.B. Lugão, PVGA/Alginate-AgNPs hydrogel as absorbent biomaterial and its soil biodegradation behavior, Polym. Bull. 77 (2020) 4147–4166. https://doi.org/10.1007/s00289-019-02966-x.
[66] A. Taheri Najafabadi, A.A. Khodadadi, M.J. Parnian, Y. Mortazavi, Atomic layer deposited Co/γ-Al2O3 catalyst with enhanced cobalt dispersion and Fischer–Tropsch synthesis activity and selectivity, Applied Catalysis A: General 511 (2016) 31–46. https://doi.org/10.1016/j.apcata.2015.11.027.
[67] T.-D. Hoang, N. Nghiem, Recent Developments and Current Status of Commercial Production of Fuel Ethanol, Fermentation 7 (2021) 314. https://doi.org/10.3390/fermentation7040314.
[68] E. Newes, C. Clark, L. Vimmerstedt, S. Peterson, D. Burkholder, D. Korotney, D. Inman, Expanding Ethanol Production in the United States: The Roles of Policy, Price, and Demand, Energy Policy 161 (2021) 1–10. https://doi.org/10.1016/j.enpol.2021.112713.
[69] J. Areola Hernandez, G.S. Uddin, A. Dutta, A. Ahmed, S.H. Kang, Are ethanol markets globalized or regionalized?, Physica A: Statistical Mechanics and its Applications 551 (2020) 124094. https://doi.org/10.1016/j.physa.2019.124094.
[70] A. Bastianin, M. Galeotti, M. Manera, Causality and predictability in distribution: The ethanol–food price relation revisited, Energy Economics 42 (2014) 152–160. https://doi.org/10.1016/j.eneco.2013.12.014.
[71] P.H. Hoeckel, A.M. Alvim, J.P. Pontes, J. Dias, The Ethanol Market and Its Relation to the Price of Agricultural Commodities, Energies 16 (2023) 2788. https://doi.org/10.3390/en16062788.
[72] A.S. Nascimento Filho, H. Saba, R.G.O. dos Santos, J.G.A. Calmon, M.L.V. Araújo, E.M.F. Jorge, T.B. Murari, Analysis of Hydrous Ethanol Price Competitiveness after the Implementation of the Fossil Fuel Import Price Parity Policy in Brazil, Sustainability 13 (2021) 9899. https://doi.org/10.3390/su13179899.
[73] T. Mizik, L. Nagy, Z. Gabnai, A. Bai, The Major Driving Forces of the EU and US Ethanol Markets with Special Attention Paid to the COVID-19 Pandemic, Energies 13 (2020) 5614. https://doi.org/10.3390/en13215614.
[74] K. Guan, J. Shen, G. Liu, J. Zhao, H. Zhou, W. Jin, Spray-evaporation assembled graphene oxide membranes for selective hydrogen transport, Separation and Purification Technology 174 (2017) 126–135. https://doi.org/10.1016/j.seppur.2016.10.012.
[75] Y. Luo, J. Zhang, Z. Zhou, J.P. Aguilar-Lopez, R. Greco, T. Bogaard, Effects of dynamic changes of desiccation cracks on preferential flow: experimental investigation and numerical modeling, Hydrol. Earth Syst. Sci. 27 (2023) 783–808. https://doi.org/10.5194/hess-27-783-2023.
[76] J. Islam, B.S. Yoon, P.T. Thien, C.H. Ko, S.-K. Kim, Enhancing oxygen evolution reaction performance in PEM water electrolyzers through support pore structure optimization, Catalysis Today 425 (2024) 114349. https://doi.org/10.1016/j.cattod.2023.114349.

[77] Y. Li, Z. Kan, L. Jia, D. Zhang, Y. Hong, J. Liu, H. Huang, S. Li, S. Liu, Elucidating the Role of Mass Transfer in Electrochemical Redox Reactions on Electrospun Fibers, Trans. Tianjin Univ. 29 (2023) 313–320. https://doi.org/10.1007/s12209-023-00369-8.
[78] K. Tsuburaya, K. Obata, K. Nagato, K. Takanabe, Porous Substrate Optimization for Efficient Water Electrolysis: Uncovering Electrocatalysts, Electrolyte, and Bubble Dynamics Effects, ACS Sustainable Chem. Eng. 12 (2024) 16308–16319. https://doi.org/10.1021/acssuschemeng.4c05790.
[79] A. Vazhayil, J. Thomas, N. Thomas, Cobalt doping in LaMnO3 perovskite catalysts – B site optimization by solution combustion for oxygen evolution reaction, Journal of Electroanalytical Chemistry 918 (2022) 116426. https://doi.org/10.1016/j.jelechem.2022.116426.
[80] X. Liu, H. Gong, T. Wang, H. Guo, L. Song, W. Xia, B. Gao, Z. Jiang, L. Feng, J. He, Cobalt-Doped Perovskite-Type Oxide LaMnO3 as Bifunctional Oxygen Catalysts for Hybrid Lithium-Oxygen Batteries, Chem. Asian J. 13 (2018) 528–535. https://doi.org/10.1002/asia.201701561.
[81] W.G. Hardin, J.T. Mefford, D.A. Slanac, B.B. Patel, X. Wang, S. Dai, X. Zhao, R.S. Ruoff, K.P. Johnston, K.J. Stevenson, Tuning the Electrocatalytic Activity of Perovskites through Active Site Variation and Support Interactions, Chem. Mater. 26 (2014) 3368–3376. https://doi.org/10.1021/cm403785q.
[82] H. He, J. Chen, D. Zhang, F. Li, X. Chen, Y. Chen, L. Bian, Q. Wang, P. Duan, Z. Wen, X. Lv, Modulating the Electrocatalytic Performance of Palladium with the Electronic Metal–Support Interaction: A Case Study on Oxygen Evolution Reaction, ACS Catal. 8 (2018) 6617–6626. https://doi.org/10.1021/acscatal.8b00460.
[83] Yun Bao, Kensaku Nagasawa, Yoshiyuki Kuroda, Shigenori Mitsushima, Current Measurement and Electrochemical Characterization of Gas Evolution Reactions on a Rotating Ring-Disk Electrode, Electrocatalysis 11 (2020) 301–308. https://doi.org/10.1007/s12678-020-00589-9.
[84] A.R.C. Bredar, A.L. Chown, A.R. Burton, B.H. Farnum, Electrochemical Impedance Spectroscopy of Metal Oxide Electrodes for Energy Applications, ACS Appl. Energy Mater. 3 (2020) 66–98. https://doi.org/10.1021/acsaem.9b01965.
[85] V. Tripkovic, H.A. Hansen, J.M. Garcia-Lastra, T. Vegge, Comparative DFT+U and HSE Study of the Oxygen Evolution Electrocatalysis on Perovskite Oxides, J. Phys. Chem. C 122 (2018) 1135–1147. https://doi.org/10.1021/acs.jpcc.7b07660.
[86] E. Budiyanto, S. Salamon, Y. Wang, H. Wende, H. Tüysüz, Phase Segregation in Cobalt Iron Oxide Nanowires toward Enhanced Oxygen Evolution Reaction Activity, JACS Au 2 (2022) 697–710. https://doi.org/10.1021/jacsau.1c00561.
[87] J. Knöppel, M. Möckl, D. Escalera-López, K. Stojanovski, M. Bierling, T. Böhm, S. Thiele, M. Rzepka, S. Cherevko, On the limitations in assessing stability of oxygen evolution catalysts using aqueous model electrochemical cells, Nat. Commun. 12 (2021) 2231. https://doi.org/10.1038/s41467-021-22296-9.
[88] L. An, R. Chen, Y. Li (Eds.), Flow Cells for Electrochemical Energy Systems: Fundamentals and Applications, 1st ed., Springer International Publishing; Imprint Springer, Cham, 2023.
[89] C. Li, J.-B. Baek, The promise of hydrogen production from alkaline anion exchange membrane electrolyzers, Nano Energy 87 (2021) 106162. https://doi.org/10.1016/j.nanoen.2021.106162.

[90] R. Baddour-Hadjean, J.-P. Pereira-Ramos, Raman microspectrometry applied to the study of electrode materials for lithium batteries, Chem. Rev. 110 (2010) 1278–1319. https://doi.org/10.1021/cr800344k.
[91] H.R. Barai, A.N. Banerjee, S.W. Joo, Improved electrochemical properties of highly porous amorphous manganese oxide nanoparticles with crystalline edges for superior supercapacitors, Journal of Industrial and Engineering Chemistry 56 (2017) 212–224. https://doi.org/10.1016/j.jiec.2017.07.014.
[92] N.S. Chaudhari, S.S. Warule, S. Muduli, B.B. Kale, S. Jouen, B. Lefez, B. Hannoyer, S.B. Ogale, Maghemite (hematite) core (shell) nanorods via thermolysis of a molecular solid of Fe-complex, Dalton Trans. 40 (2011) 8003–8011. https://doi.org/10.1039/c1dt10319a.
[93] S.P. Schwaminger, P. Fraga-García, F. Selbach, F.G. Hein, E.C. Fuß, R. Surya, H.-C. Roth, S.A. Blank-Shim, F.E. Wagner, S. Heissler, S. Berensmeier, Bio-nano interactions: cellulase on iron oxide nanoparticle surfaces, Adsorption 23 (2017) 281–292. https://doi.org/10.1007/s10450-016-9849-y.
[94] C. Pasquini, L. D'Amario, I. Zaharieva, H. Dau, Operando Raman spectroscopy tracks oxidation-state changes in an amorphous Co oxide material for electrocatalysis of the oxygen evolution reaction, J. Chem. Phys. 152 (2020) 194202. https://doi.org/10.1063/5.0006306.
[95] J. Huang, H. Sheng, R.D. Ross, J. Han, X. Wang, B. Song, S. Jin, Modifying redox properties and local bonding of Co3O4 by CeO2 enhances oxygen evolution catalysis in acid, Nat. Commun. 12 (2021) 3036. https://doi.org/10.1038/s41467-021-23390-8.
[96] F. Bai, J. Schulwitz, T. Priamushko, U. Hagemann, A. Kostka, M. Heidelmann, S. Cherevko, M. Muhler, T. Li, Correlating atomic-scale structural and compositional details of Ca-doped LaCoO3 perovskite nanoparticles with activity and stability towards the oxygen evolution reaction, Journal of Catalysis 438 (2024) 115697. https://doi.org/10.1016/j.jcat.2024.115697.
[97] W. Hu, Q. Liu, T. Lv, F. Zhou, Y. Zhong, Impact of interfacial CoOOH on OER catalytic activities and electrochemical behaviors of bimetallic CoxNi-LDH nanosheet catalysts, Electrochimica Acta 381 (2021) 138276. https://doi.org/10.1016/j.electacta.2021.138276.
[98] Z. Li, Y. Xie, Z. Huang, Y. Su, C. Sun, J. Fu, H. Wei, F. Wu, G. Ou, Amorphization of LaCoO 3 Perovskite Nanostructures for Efficient Oxygen Evolution, ACS Appl. Nano Mater. 5 (2022) 14209–14215. https://doi.org/10.1021/acsanm.2c02982.
[99] W. Cai, R. Chen, H. Yang, H.B. Tao, H.-Y. Wang, J. Gao, W. Liu, S. Liu, S.-F. Hung, B. Liu, Amorphous versus Crystalline in Water Oxidation Catalysis: A Case Study of NiFe Alloy, Nano Lett. 20 (2020) 4278–4285. https://doi.org/10.1021/acs.nanolett.0c00840.
[100] A. Indra, P.W. Menezes, N.R. Sahraie, A. Bergmann, C. Das, M. Tallarida, D. Schmeißer, P. Strasser, M. Driess, Unification of catalytic water oxidation and oxygen reduction reactions: amorphous beat crystalline cobalt iron oxides, J. Am. Chem. Soc. 136 (2014) 17530–17536. https://doi.org/10.1021/ja509348t.
[101] J. Wang, X. Ma, F. Qu, A.M. Asiri, X. Sun, Fe-Doped Ni2P Nanosheet Array for High-Efficiency Electrochemical Water Oxidation, Inorg. Chem. 56 (2017) 1041–1044. https://doi.org/10.1021/acs.inorgchem.6b02808.
[102] F. Bao, E. Kemppainen, I. Dorbandt, F. Xi, R. Bors, N. Maticiuc, R. Wenisch, R. Bagacki, C. Schary, U. Michalczik, P. Bogdanoff, I. Lauermann, R. van de Krol, R. Schlatmann, S. Calnan, Host, Suppressor, and Promoter—The Roles of Ni and Fe on Oxygen Evolution Reaction Activity and Stability of NiFe Alloy Thin Films in Alkaline Media, ACS Catal. 11 (2021) 10537–10552. https://doi.org/10.1021/acscatal.1c01190.

[103] C. Lv, H. Chen, M. Hu, T. Ai, H. Fu, Nano-oxides washcoat for enhanced catalytic oxidation activity toward the perovskite-based monolithic catalyst, Environ. Sci. Pollut. Res. Int. 28 (2021) 37142–37157. https://doi.org/10.1007/s11356-021-13354-2.

Graphical abstract

The comparison study of lanthanum-based perovskites reveals that it is essential to combine lab-scale and application-relevant electrochemical analysis. Only in that case it is possible to get a complete picture of how to develop electrocatalysts further. This systematic assessment can be achieved by the implementation of a highly structured, coherent workflow that enables a rapid material evaluation and transition from academic research to industrial development.